Thermally Induced Compression Waves and Gravity Waves Generated by Convective Storms

MELVILLE E. NICHOLLS AND ROGER A. PIELKE SR.

Department of Atmospheric Science, Colorado State University, Fort Collins, Colorado

(Manuscript received 15 May 1998, in final form 17 November 1999)

ABSTRACT

A three-dimensional, fully compressible cloud model is used to simulate a convective storm in order to investigate the properties of compression waves and gravity waves induced by latent heat release. Time series of the low-level pressure perturbations caused by the propagating waves are examined at various distances from the storm. A compression wave that is close to hydrostatic balance and can be considered to be a Lamb wave, which propagates in the horizontal plane, emerges from the storm. This latter property gives the wave a distinctly two-dimensional character that is clarified by comparison with a linear model of a two-dimensional thermally induced compression wave. This has implications for its shape and results in a decay rate with distance propagated from the source of $1/(\text{distance})^{1/2}$. The period of the Lamb wave is determined primarily by the time it takes for the storm to develop and decay. The fast-moving Lamb wave is trailed by slower-moving thermally induced gravity waves. It is found that the amplitude of the gravity waves decay with 1/distance. Distinct gravity wave modes can be identified. The first mode propagates the fastest and results in deep subsidence warming. The second mode propagates at half the speed of the first and causes weak low-level uplift, which in some convective situations might aid the development of new convection.

An analysis of the transfer of internal and gravitational potential energies showed that the net transfer by the Lamb wave was approximately equal to the net increase of total energy in the atmosphere brought about by the convective storm. This result suggests that physical interpretations of total energy transfer in the atmosphere need to take into account that it can be transferred in a wavelike manner at the speed of sound.

An interesting buoyancy oscillation occurred when the downdraft air overshot its buoyant equilibrium level, which resulted in a resurgence of convection. The convection was able to obtain moderate strength by feeding on moist environmental air that had been advected over the top of the cold pool. This mechanism may be a factor contributing to the early meso-β convective cycle that has been observed in many convective systems.

1. Introduction

The three types of wave solutions to the linearized equations for a stratified fluid are known as acoustic waves, Lamb waves, and gravity waves (see, e.g., Gill 1982). The restoring force for acoustic and Lamb waves is compression, whereas for gravity waves the restoring force is buoyancy. Latent heat release in a convective storm generates all three types. This study focuses on low-frequency Lamb waves and gravity waves generated by latent heat release in a convective storm.

Thermally induced compression waves are of theoretical interest since they transfer total energy at the speed of sound (Nicholls and Pielke 1994a and 1994b, hereafter referred to as NPa and NPb, respectively). Therefore a complete physical interpretation of total energy transport requires an understanding that sensible energy and gravitational potential energy can be transferred very quickly at the speed of sound in a wavelike manner, rather than in a slower advective manner, which, for instance, would be the main way that latent energy associated with water vapor would be transferred. This total energy composed of kinetic energy, internal energy, gravitational potential energy, and latent energy should be clearly distinguished from perturbation energy, or wave energy composed of kinetic energy and available potential energy (see, e.g., Gill 1982). [The available potential energy is itself composed of two terms, which Eckart (1960) calls thermobaric and elastic energies.] A thermally induced compression wave is generated when a parcel of air is heated. The pressure increases within the air parcel causing it to expand and adjacent air to be compressed, which generates a compression wave. Work is done in compressing the adjacent air. Both the density and temperature increase in the compressed air leading to increases in internal and gravitational potential energies per unit volume (NPa). These changes in density and temperature associated with a compression wave generated by a convective

Corresponding author address: Dr. Melville Nicholls, Dept. of Atmospheric Science, Colorado State University, Fort Collins, CO 80523.
E-mail: nicholl@nebula.atmos.colostate.edu

storm are very small and correspondingly the changes in internal and gravitational potential energies per unit volume at any particular location in the wave are also very small. However, since the wave front propagates very quickly resulting in compression of air over an extremely large volume, the net change in internal and gravitational potential energies adds up to a substantial amount. In this study, it is found that it is approximately equal to the net latent heat release by the storm. Of course, the kinetic energy within the storm due to the strong motions is far more meteorologically significant, even though the kinetic energy generated is very small compared to the net increase in internal and gravitational potential energies (NPa). Although the transfer of internal and gravitational potential energies by compression waves may not be of great meteorological significance, the role that they have in this process should at least be recognized and taken into account in physical interpretations of total energy transfer. A possible practical application is that if such waves could be detected they might be used to infer the location and intensity of thunderstorms (Pielke et al. 1993). In this study, we investigate the amplitude, structure, and decay rate of Lamb waves generated in numerical simulations of convective storms and suggest possible ways of detecting them.

The role of gravity waves in a two-dimensional simulation of a cloud has been investigated by Bretherton and Smolarkiewicz (1989). They found that the spreading gravity waves adjusted the environmental buoyancy to be equal to the cloud buoyancy by compensating subsidence. Schmidt and Cotton (1990) studied the interaction between upper- and lower-tropospheric gravity waves in a two-dimensional simulation of a squall line. The environment consisted of three distinct thermodynamic layers. They found that with vertical wind shear, sustained coupling between the upper and lower waves could occur, which was crucial for the maintenance of the squall line. Also, the importance of thermally induced gravity waves for understanding the structure of squall lines has recently been emphasized by Pandya and Durran (1996). A two-dimensional linearized model was constructed by Nicholls et al. (1991a) to study the gravity waves generated by prescribed heat sources representing both convective and stratiform regions of mesoscale convective systems (MCSs). The prescribed vertical heating profile for a convective region was approximated by a half-sine wave through the depth of the troposphere. For a stratiform region a combination of a half-sine wave and a full-sine wave of opposite sign was used. Generally, the solution can be obtained for heating profiles given by combinations of $\sin(n\pi z/H)$, where z is height, H the height of the tropopause, and n can be considered the order of the gravity wave mode, which is excited. The speed of the gravity wave mode for the case of a rigid lid at $z = H$ is $c = NH/n\pi$ where N is the buoyancy frequency. For $N = 10^{-2}$ and $H = 10$ km, the $n = 1$ mode has a speed of 30 m s^{-1} and the $n = 2$ mode a speed of 15 m s^{-1} (hereafter, the $n = 1$ and $n = 2$ modes are abbreviated to $n1$ and $n2$ modes, respectively). The $n1$ mode was considered to be the primary mode responsible for deep compensating subsidence warming and mesolows produced by deep convection, whereas, the $n2$ mode was considered to be associated with midlevel inflow and to be forced by a change in the heating profile later on in the system lifetime caused primarily by low-level evaporational cooling. Additionally, a solution was obtained for a heating that was turned off after some time producing two oppositely moving gravity wave rolls. This latter solution was qualitatively similar to gravity waves produced in a two-dimensional numerical simulation of a Florida thunderstorm by Nicholls et al. (1991b). Nicholls et al. (1991a) and Pandya et al. (1993) also considered the case of a semiinfinite region. Although gravity wave energy could now propagate upward a distinct modal structure similar to the rigid-lid case was still evident. The magnitude of the compensating subsidence for the $n1$ mode was, however, significantly less than for the rigid-lid case (Pandya et al. 1993). Mapes (1993) emphasized that the combined effect of the $n1$ and $n2$ modes is to cause upward displacements at low levels in the nearby atmosphere thus favoring the development of additional convection nearby. This possibility was also explored by McAnelly et al. (1997), who suggested that the upscale development of a MCS might sometimes be caused by this process. Their observations suggest that after the early convection decays it is followed an hour or two later by a reintensification on a larger scale. Results of an observational study led Johnson et al. (1995) to suggest that convectively generated gravity waves may have been responsible for the rising and strengthening of an inversion in the gap between two MCSs, which effectively capped vigorous congestus clouds that had developed.

To date there have not been any observational experiments designed explicitly to detect the transient $n1$ and $n2$ thermally induced gravity wave modes in the atmosphere. The $n1$ mode clearly plays an important role in stabilizing the environment. The mesolows adjacent to convective systems are evidence of the existence of this mode. Although, it shows up in time series of surface pressure traces its structure and decay rate have not been systematically investigated. The same thing is true of the $n2$ mode, which may play an important role in some situations by causing low-level uplift, which destabilizes the atmosphere. All the previous studies mentioned have had the limitation of being two dimensional. In this study, we look at the gravity waves produced in a three-dimensional framework, which has important implications for their structure and decay rate. The numerical modeling results should aid in comprehending observations of thermally induced gravity waves.

In section 2, hydrostatic adjustment by acoustic waves is discussed and a linear model of a thermally induced

compression wave is developed that gives insight into its structure and how it decays with distance traveled from the source. The numerical cloud model used in this study is discussed in section 3. A description of the experiments is given in section 4 and results are presented in section 5. Conclusions and possible methods that could be employed to detect thermally induced compression waves and gravity waves are discussed in section 6.

2. Hydrostatic adjustment and a linear model of a thermally induced compression wave

To understand the results of the numerical simulations, it is helpful to first discuss hydrostatic adjustment and to present results of a linear model of a thermally induced compression wave. To simplify the mathematical analysis for the linear model the gravitational force is neglected. The solutions we will obtain are similar to those obtained for sound waves generated by sources of mass outflow (see, e.g., Lighthill 1978). These solutions show that the shape of the generated sound wave and its decay rate with distance traveled depend on whether the wave propagates in one dimension, two dimensions, or three dimensions. If we consider a convective rainstorm, the latent heat release generates an approximately spherical acoustic wave front. The downward-propagating part reflects off the ground and then propagates into the upper atmosphere. The much simpler case of acoustic waves produced by a horizontally infinite heated layer and the resultant adjustment to a new hydrostatic balance has been investigated by Bannon (1995, 1996) as an extension to the work of Lamb (1908, 1932). NPb showed that surface heat fluxes on an island will generate Lamb waves, which propagate offshore at the speed of sound. To clarify further how Lamb waves are generated and to show the relation to these previous studies on hydrostatic adjustment we conducted a simple two-dimensional experiment using a fully compressible model for an isothermal atmosphere. The experiment was similar to the one conducted by Bannon (1995), except that a column of the atmosphere was heated at low levels, which was separated from the undisturbed environment by removable walls (see, e.g., Nicholls et al. 1993, for discussion of wall boundary conditions). The heating was turned on for a short time and generated vertically propagating acoustic waves, which were modified by gravity. The final adjusted hydrostatic state in the column showed a positive pressure perturbation both in and above the heated layer with a maxima at the top of the layer similar to Fig. 2 of Bannon (1995) and Fig. 7 of NPb. When the walls were removed the pressure gradient existing between the air in the column and the adjacent environmental air on either side generated two oppositely moving Lamb waves. As the Lamb waves propagated away, buoyancy of air in the column led to the generation of gravity waves. For the more realistic situation of this study a rather complicated adjustment occurs close to the storm since acoustic waves are not constrained only to vertical propagation. Nevertheless, they still bring about adjustments of air columns toward a new hydrostatic balance. A few tens of kilometers from the storm a compression wave emerges, which is close to a hydrostatic balance and hence essentially a Lamb wave, which propagates only in the horizontal plane. In this study, we do not concern ourselves with the details of the complex adjustment process close to the storm, but instead examine the properties of the Lamb wave that emerges. Since the wave propagates only in the horizontal plane, it has properties of a two-dimensionally propagating wave. We illustrate these properties by deriving the solution for a two-dimensional thermally induced compression wave. The linearized momentum, continuity, and thermodynamic equations are:

$$\rho_0 \frac{\partial}{\partial t}\mathbf{u} + \nabla p' = 0, \tag{1}$$

$$\frac{1}{\rho_0}\frac{\partial \rho'}{\partial t} + \nabla \cdot \mathbf{u} = 0, \tag{2}$$

$$\frac{\partial p'}{\partial t} - c^2 \frac{\partial \rho'}{\partial t} = \frac{\rho_0 c^2}{c_p T_0} Q_m, \tag{3}$$

where $\mathbf{u}$ is velocity, p pressure, ρ density, T temperature, Q_m the heating rate per unit mass, c_p the specific heat at constant pressure, and c the speed of sound. A zero subscript denotes the basic state and a prime a perturbation from the basic state. These equations can be manipulated to obtain a single equation for p':

$$\frac{\partial^2 p'}{\partial t^2} - c^2 \nabla^2 p' = \frac{\rho_0 c^2}{c_p T_0}\frac{\partial Q_m}{\partial t}. \tag{4}$$

A one-dimensional solution to this equation was obtained by NPa. In the appendix, the two-dimensional solution is obtained, as well as the three-dimensional solution, for a heating function of the form $Q_m = Q_0 P(t) b^4/(r^2 + b^2)^2$, where Q_0 is a constant, b is the width at which the heating is a quarter of the maximum value, and r is the distance from the center of the source. The pulse function $P(t) = 1$ for $a < t < a + \epsilon$ and 0 otherwise where a is the time at which the pulse commences and ϵ the duration of the pulse. Solutions for heat sources, which are arbitrary functions of time, can be obtained by summing up a series of short duration pulses.

Figure 1 shows results for a heating function constructed from a series of pulses, which varies with time as $\tau^2/[(t - t_0)^2 + \tau^2]$ where t_0 is the time at which the heating is a maximum, taken to be 1800 s, $\tau = 5$ min, $b = 5$ km, $Q_0 = 1$ J kg^{-1} s^{-1}, $T_0 = 280$ K, $\rho_0 = 1$ kg m^{-3}, and $r = 100$ km, for the one-, two-, and three-dimensional cases, respectively. These results are very similar to those shown by Lighthill (1978; Fig. 1) for sound waves produced by a source of mass outflow. They show that a positive heat pulse produces a positive

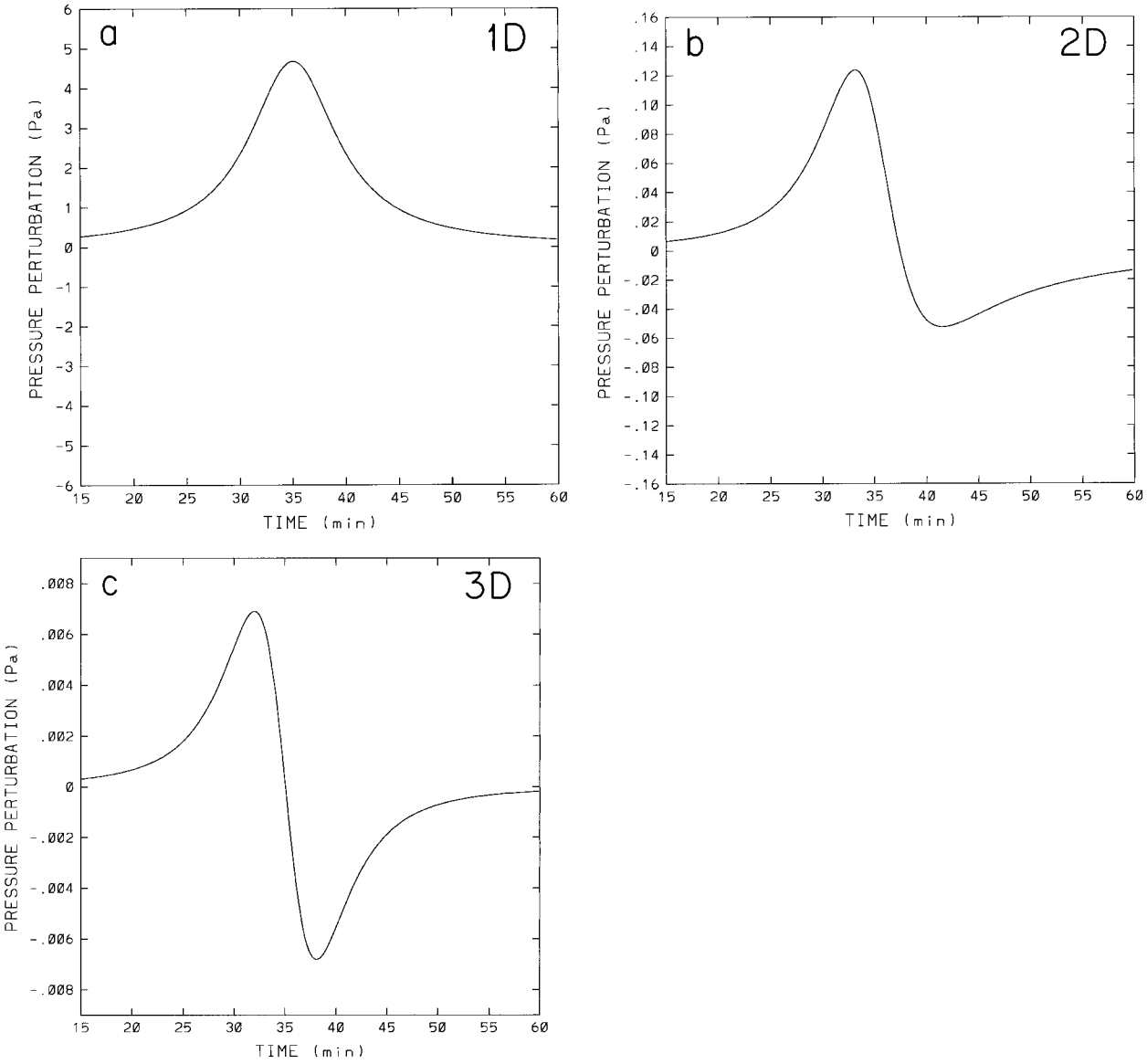

FIG. 1. Results of the linear model of a thermally induced compression wave for (a) one dimension, (b) two dimensions, and (c) three dimensions.

pressure pulse in one dimension, but a quite different shaped pressure pulse in two and three dimensions. Instead of a purely positive pressure pulse in two dimensions, a deep short positive lobe is followed by an extended, but shallower negative lobe of the same total area. In three dimensions, a deep short positive lobe is followed by an identical negative lobe. In one dimension, the amplitude of the pressure perturbations do not decay with distance traveled from the source, whereas in two dimensions they decay as 1/(distance)$^{1/2}$ and in three dimensions as 1/distance. Figure 2 shows the two- and three-dimensional solutions for a constant heating rate of duration 5 min. This case is of interest since the simulated convective storms in this study are initialized by a warm bubble produced by a steady heating applied for a duration of 5 min, which also generates a compression wave. Both cases have short positive and negative lobes, but in the two-dimensional case there is a more gradual decrease in the amplitude of the lobes.

3. Model

The model used in this study differs from the version used in NPa and NPb since the Exner function [$\Pi = (p/pr)^{R/c_p}$, where p is pressure, p_r a reference pressure, R the gas constant, and c_p the specific heat capacity at constant pressure] is used as a predictive variable instead of density. This approach conforms with that used in the standard version of the Regional Atmospheric Modeling System (RAMS) and enables the use of the

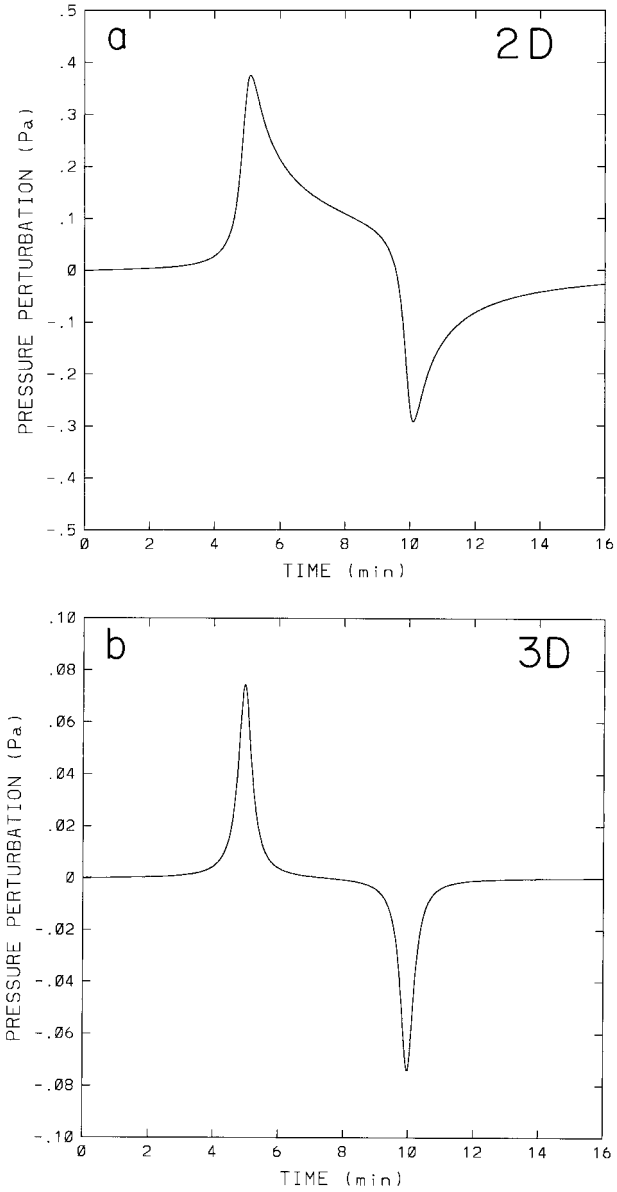

FIG. 2. Results of the linear model for a constant heating rate of duration 5 min for (a) two dimensions, and (b) three dimensions.

various options that are available. For the standard version of RAMS certain terms are neglected from the prognostic equation for the Exner function, which has the effect of eliminating thermally induced compression waves. This is done for computational efficiency as discussed by Klemp and Wilhelmson (1978). Instead of including the terms neglected in Eq. (2.7) of Klemp and Wilhelmson (1978), the prognostic equation for the Exner function is reformulated in a simpler form, as follows.

The ideal gas law can be written

$$p = \rho RT(1 + 0.61w), \tag{5}$$

where ρ is density, T is temperature, and w the mixing ratio of water vapor. Substituting $p = p_r\Pi^{1/\kappa}$ and $T = \theta\Pi$, where $\kappa = R/c_p$, and θ is potential temperature, gives

$$p_r\Pi^{c_v/R} = \rho R\theta_v, \tag{6}$$

where $\theta_v = \theta(1 + 0.61w)$ is the virtual potential temperature. Taking the local derivative of Eq. (6) with respect to time and using the equation of continuity for moist air with a mass source S added to account for phase changes from water to vapor, gives

$$p_r\frac{c_v}{R}\Pi^{c_v/R-1}\frac{\partial\Pi}{\partial t} = -R\theta_v[\nabla\cdot(\rho\mathbf{u}) - S] + \rho R\frac{\partial\theta_v}{\partial t}, \tag{7}$$

where c_v is the specific heat capacity at constant volume and $\mathbf{u}$ velocity. Decomposition of the Exner function into a base state and a perturbation, $\Pi = \Pi_o(z) + \Pi'(x, y, z)$ and rearrangement of the constants, gives

$$\frac{\partial\Pi'}{\partial t} = \frac{-R\Pi}{c_v\rho}[\nabla\cdot(\rho\mathbf{u}) - S] + \frac{R\Pi}{c_v\theta_v}\frac{\partial\theta_v}{\partial t}. \tag{8}$$

In addition to this prognostic equation for the perturbation Exner function the model also has prognostic equations for the three components of momentum, a thermodynamic equation, and a set of microphysics equations (Pielke et al. 1992; Walko et al. 1995). The microphysics categories are: cloud droplets, rain, pristine ice, snow, aggregates, graupel, and hail. Cloud droplets are monodispersed with a number concentration specified in this study to be 3×10^8 m^{-3}. The number of pristine ice crystals is prognosed. Other species are assumed to have a Marshall–Palmer distribution (Kessler 1969) with a mean mass diameter of 1 mm. Subgrid-scale fluxes are modeled by a Smagorinsky-type scheme with a Richardson number dependence (Tripoli and Cotton 1986). The equations are solved on an Arakawa C grid. A split time-differencing scheme is used, unlike the approach of NPa and NPb so that acoustic terms are computed separately for computational efficiency (Klemp and Wilhelmson 1978; Tripoli and Cotton 1982; Skamarock and Klemp 1992). As a check of this method a simulation of a Lamb wave by NPb was repeated using this time-split approach and found to give nearly identical results. For this study the time-split scheme used three small time steps per one long time step. Velocity components and pressure are updated using leapfrog differencing and all other variables are advanced using forward differencing on the long time step. A forward–backward scheme is used on the small time step (Tripoli and Cotton 1982). A second-order-in-space advection scheme is employed. The model has nested grid capability, and for the three-dimensional simulations performed in this study, four grids were used. The horizontal grid increments were 27, 9, 3, and 1 km. The number of horizontal grid points were 80×80 for the coarsest grid, 59×59 for the second and third grids, and 80×80 for the finest grid. Each nested grid was

centered within the next coarsest grid. Periodic lateral boundary conditions were employed for the coarsest grid. This was because when radiative boundary conditions were used in conjunction with a vertically sheared initial wind profile it was found that small pressure perturbations were generated at the boundaries comparable in magnitude to the thermally induced compression waves. A large domain was required so that the compression wave could be observed at large distances from the storm by which time it had outdistanced the slower-moving gravity waves. Also, a larger domain was used so that waves would not have time to travel back into the center of the domain during the simulation because of the periodic boundary conditions. The vertical grid increment was 400 m at the surface and was gradually stretched with height to a maximum of 2.5 km. There were 50 vertical grid points and the model top was at 80 km above the surface. A Rayleigh friction layer 35 km in depth was employed in the upper portion of the model domain in order to reduce reflection of the compression waves and gravity waves from the rigid lid. A high model top was used in order to realistically simulate the Lamb wave, which has a large *e*-folding scale ($\sim$11 km) and because of the deep Rayleigh friction layer. This was important for obtaining accurate surface pressures.

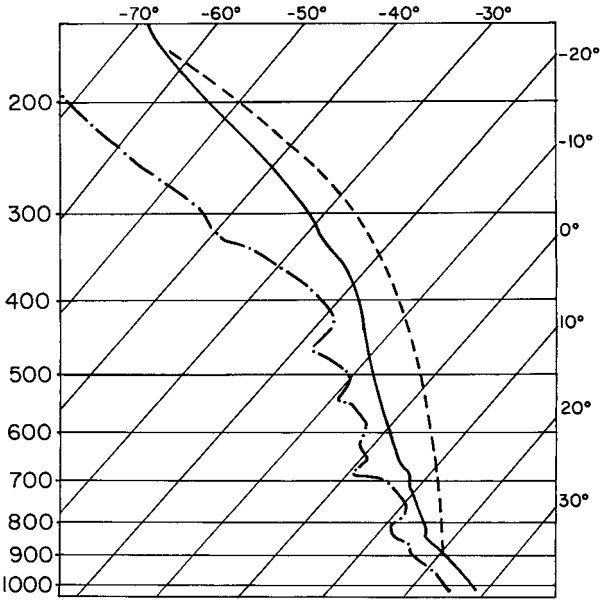

FIG. 3. Temperature (solid line) and dewpoint (dash–dot line) temperatures used to initialize the numerical model. A moist adiabat is shown by the dashed line.

4. Description of experiments

The thermodynamic profile used in these experiments is based on soundings from 17 July 1973 during the Florida Area Cumulus Experiment. This day has also been investigated by Tripoli and Cotton (1980) and Nicholls et al. (1991b). The profile used is shown in Fig. 3. The temperature has been made closer to adiabatic near the surface than used in the previous studies, in order to be more representative of the conditions later on in the day after surface heating has occurred. Above 150 mb the U.S. Standard Atmosphere temperature profile was used (see, e.g., Wallace and Hobbs 1977). The convective rainstorm was initiated by prescribing a low-level heating for 5 min in the center of the finest grid with the same horizontal structure as used for the linear model discussed in section 2 and a half-sine wave in the vertical.

Two main simulations were carried out: one with a quiescent environment and one with vertically sheared environmental winds. For this latter case, the horizontally homogeneous winds varied from -2 m s^{-1} (easterlies) at the surface linearly with height to a value of 16 m s^{-1} (westerlies), at 12 km above the surface. These simulations with the fully compressible version of the model were run for 90 min. Time series of the pressure perturbation from the initial state were written out at the first grid point above the surface ($z = 200$ m) at various locations from the storm. Additionally, some simulations were carried out with the standard version of RAMS, which will be referred to as the standard model. As discussed in section 3, the standard model does not allow the generation of thermal compression waves. For the same initialization, it does, of course, produce gravity waves that are nearly identical to those produced by the fully compressible model. These simulations were made in order to isolate the low-frequency thermal compression wave produced in the fully compressible simulations, which near the storm was superimposed with large amplitude gravity waves. Subtracting the time series of the pressure perturbations for the standard model, which only produces the large amplitude gravity waves, from that of the fully compressible model should leave the signal due to the compression wave. Also, longer duration runs with the standard model, and with fewer vertical levels, were carried out to investigate the longer-term behavior of the gravity waves. A simulation was also carried out without the microphysics to examine the waves produced by the prescribed heat source.

5. Results

a. Quiescent case

Figure 4 shows *x*–*z* cross sections of the total liquid and ice hydrometeor mixing ratio through the center of the convective storm in grid 4 at various times for the quiescent environment case. At 20 min the storm is in the early stages of development with a maximum hydrometeor mixing ratio of 6 g kg^{-1}, at $z = 4$ km. By 30 min, explosive growth has occurred with cloud top at 16.5 km and a maximum hydrometeor mixing ratio of 13 g kg^{-1} at $z = 7$ km. At 40 min, the storm is in

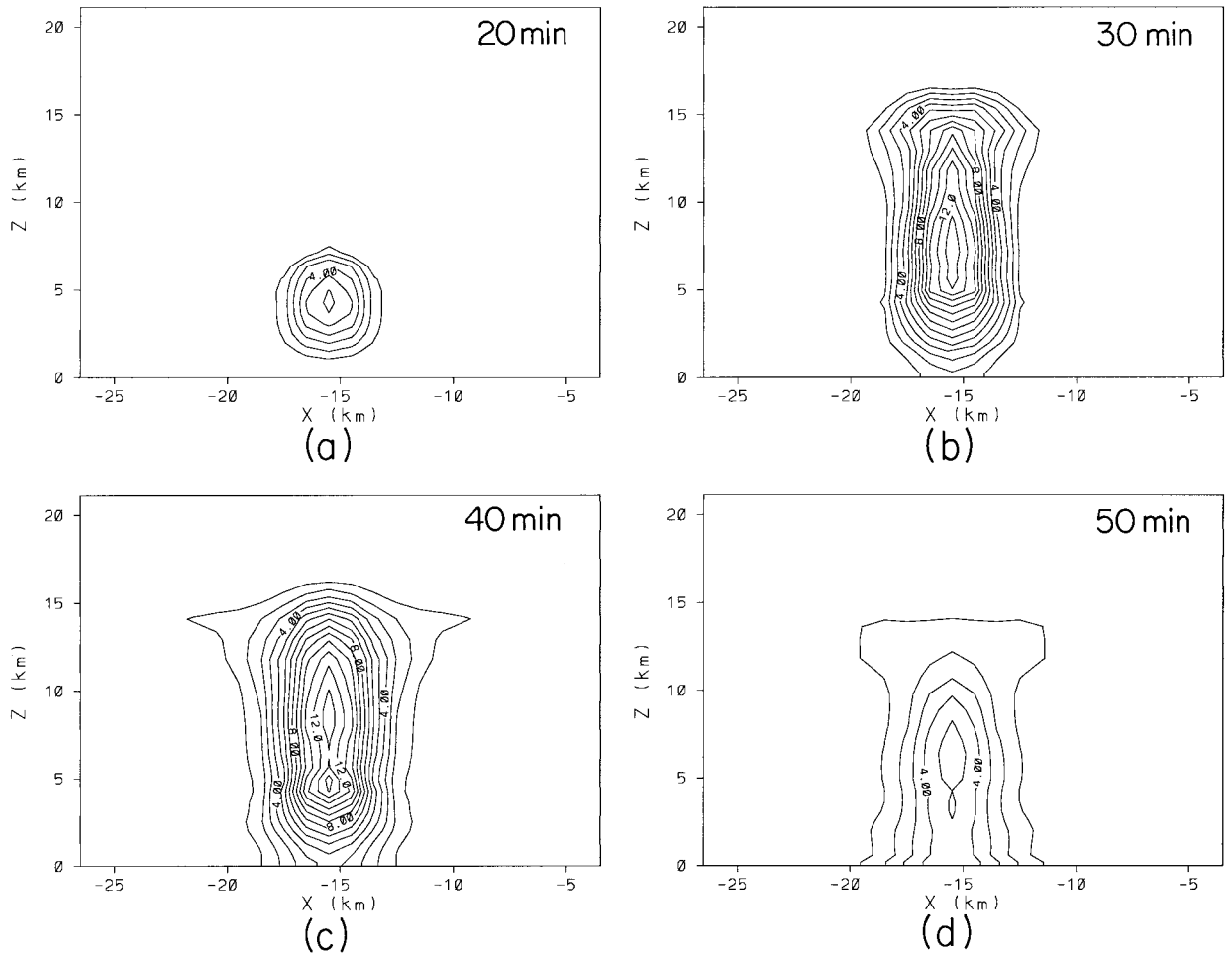

FIG. 4. Vertical cross section of the total liquid and ice hydrometeor mixing ratio for the quiescent case at (a) 20, (b) 30, (c) 40, and (d) 50 min. The contour interval is 1 g kg^{-1}.

the mature stage. Outflow at the cloud top is causing an anvil to form and precipitation is occurring at the surface. At 50 min the storm is in its decaying stage. Mixing ratios are decreasing due to hydrometeor fall out, sublimation, and evaporation. The strongest updraft occurred around 30 min at $z = 11$ km and the peak value was 39 m s^{-1}. Downdrafts driven by evaporation and waterloading began to develop beneath the updraft core at 40 min and reached a magnitude of 8 m s^{-1} at 50 min. The maximum precipitation was 52 mm and occurred at the grid point at the center of the storm.

Figure 5 shows an x–z cross section of the pressure perturbation in grid 2 through the center of the storm at 30 min. Only small magnitudes of the pressure perturbation are contoured in this figure in order to illustrate the thermally induced Lamb waves. This field is not perfectly symmetrical as are the fields in Fig. 4 since grid 4 is not exactly in the center of grids 3 and 2 and because of the interpolations used in the contouring routine. The maximum amplitude of nearly 0.6 Pa occurs at the surface at $x = -110$ and 90 km. This circular ring of high pressure propagates away from the storm at the speed of sound. The vertical structure of the pressure and density perturbations in the compression wave are approximately the same as the theoretical solution for a Lamb wave in an isothermal atmosphere (see for instance NPb). The horizontal velocity, however, did not increase with height as much as the theoretical solution. Model sensitivity tests with prescribed heating and an isothermal atmosphere gave extremely good agreement with the theoretical solution for the pressure and density perturbations. The horizontal velocity perturbations were slightly in disagreement at upper levels. Agreement was improved by eliminating Rayleigh friction in the uppermost levels. It was felt that overall the Rayleigh friction layer was of benefit to this study and that it was important to include it.

Figure 6 shows an x–z cross section of the pressure perturbation in grid 2 through the center of the storm at 50 min. This figure illustrates the $n1$ gravity wave mode with a minimum pressure of -8 Pa occurring at the surface at $x = -75$ and 45 km. This circular ring

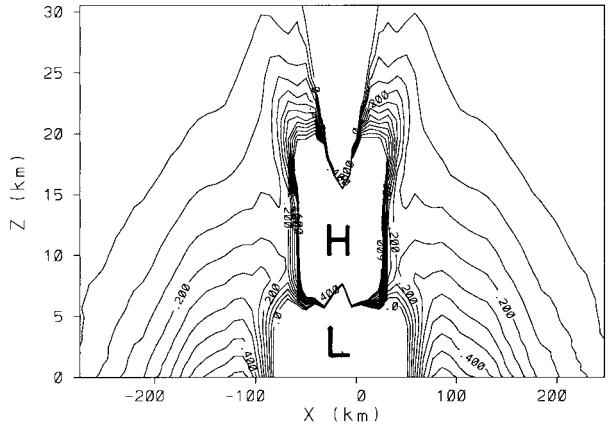

FIG. 5. Vertical cross section of the pressure perturbation in grid 2 for the quiescent case at 30 min. The contour interval is 0.05 Pa. Here H and L indicate pressure perturbations higher than 0.6 Pa and lower than 0.0 Pa, respectively.

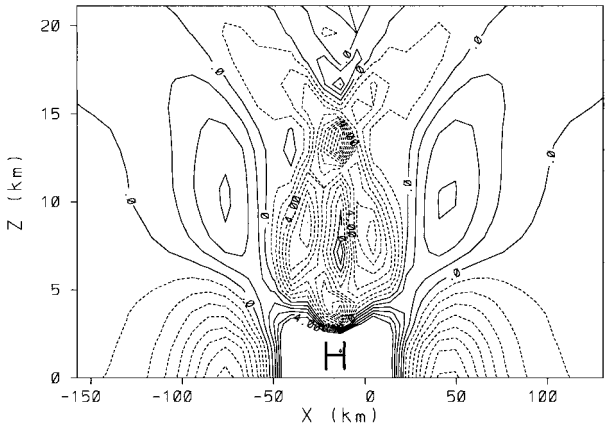

FIG. 6. Vertical cross section of the pressure perturbation in grid 2 for the quiescent case at 50 min. The contour interval is 1.0 Pa. Here H indicates pressure perturbations higher than 5.0 Pa.

of low pressure propagates away from the storm at a speed of ~48 m s^{-1}. This propagation speed is quite fast because of the high tropopause. A high pressure maximum of 3 Pa occurs at $z = 10$ km above the surface minimum. The structure of this mode in two dimensions has been discussed by Nicholls et al. (1991b) and Pandya et al. (1993). Figure 7 shows an x–z cross section of the pressure perturbation in grid 2 through the center of the storm at 80 min. This figure illustrates the $n2$ gravity wave mode with a maximum surface pressure of nearly 4.5 Pa occurring at $x = -75$ and 45 km. As discussed by Nicholls et al. (1991b), it is characterized by a surface high, a midlevel minimum, and an upper-level high. It propagates at half the speed of the $n1$ mode. At this stage it is superimposed on the tail end of the $n1$ mode. The tail end of the $n1$ mode has a pronounced positive pressure perturbation at the surface and a negative perturbation aloft, which is a major difference from the two-dimensional studies by Nicholls et al. (1991a,b). Some idealized sensitivity tests with prescribed heating suggests this behavior is mainly due to the three-dimensional geometry, rather than significant forcing of an oppositely signed $n1$ mode caused by a change in the vertical profile of the latent heating later on in the storm life cycle. Also, as will be seen, the tail end of the $n2$ mode has pressure perturbations of opposite sign than the forward part of the wave. The surface high pressure associated with the $n2$ mode is very distinct from the surface high associated with the shallow cold pool outflow between $x = -40$ and $x = 5$ km. Slower-moving high-order gravity wave modes are also evident in this figure.

Figures 8a–d show time series of the pressure perturbation at the first grid point above the surface ($z =$ 200 m) at various distances from the storm. The first pulse that occurs during the first few minutes in Fig. 8a, at 35 km from the storm in grid 4, is due to the prescribed 5-min heating used to initiate the storm. The shape of this compression wave is clearly similar to the two-dimensional solution shown in Fig. 2, not to the three-dimensional solution. This is evidence that the wave is a Lamb wave, which travels in the horizontal plane. This is then followed by a slight peak in pressure at 22 min, which is due to a low-frequency compression wave generated by the latent heat release in the storm. At this location this compression wave is superimposed on the gravity waves generated earlier by the prescribed heating as well as the leading edge of the $n1$ gravity wave mode generated by latent heat release in the storm. This makes its shape and amplitude hard to discern. Interestingly, there are small high-frequency fluctuations superimposed on the lower-frequency compression wave, which will be discussed later. The large decrease in pressure of 14.3 Pa is mainly due to the $n1$ gravity wave mode. This is followed by a large positive pressure pulse, which is a superposition of the tail end of the $n1$ mode and the forward part of the $n2$ gravity wave mode.

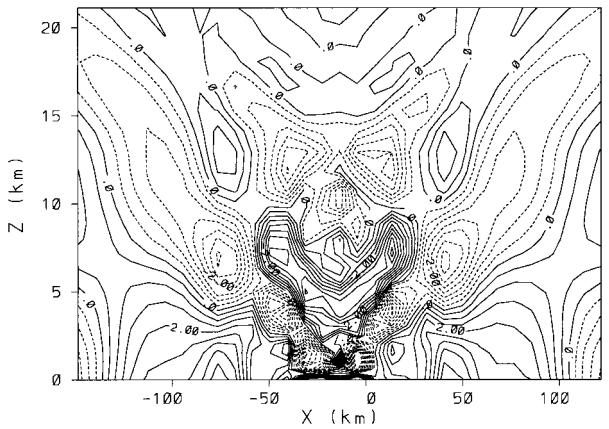

FIG. 7. Vertical cross section of the pressure perturbation in grid 2 for the quiescent case at 80 min. The contour interval is 0.5 Pa.

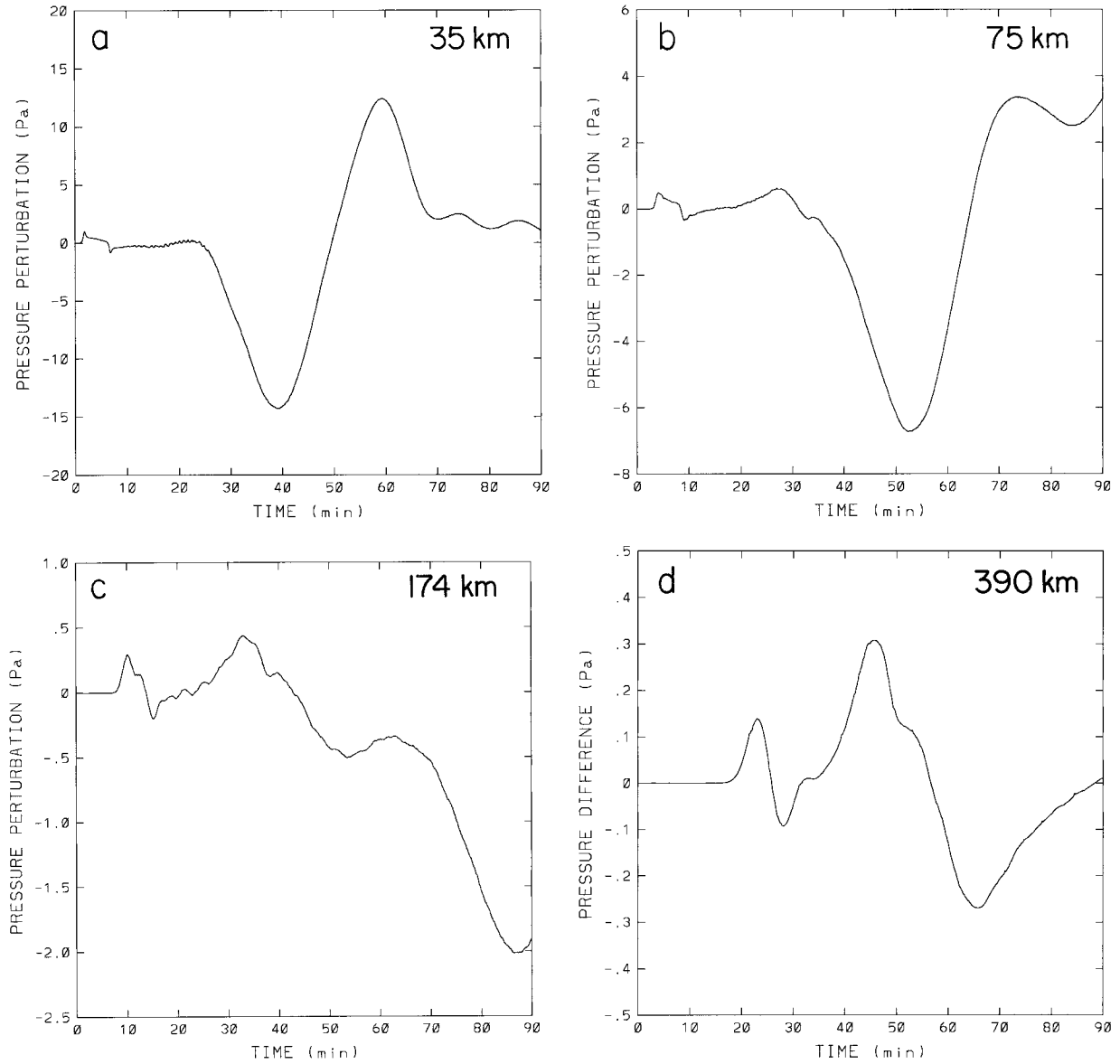

FIG. 8. Time series of the pressure perturbation near the surface for the quiescent case, at (a) 35, (b) 75, (c) 174, and (d) 390 km, from the center of the thunderstorm.

Figure 8b shows a time series of the pressure perturbation at a distance of 75 km from the center of the storm. The waves have propagated into grid 3 at this location, which results in a slight distortion of the waves. The compression wave or Lamb wave generated by latent heat release is now more evident. The positive pressure perturbation is 0.6 Pa. The amplitude of the $n1$ negative pressure perturbation is 6.8 Pa. The following positive pressure perturbation has started to separate into two maxima. The first is the positive lobe associated with the $n1$ mode and the second, which can just be seen at the edge of the figure, the forward part of the $n2$ mode. This separation of modes will be shown in more detail for longer duration runs later. Figure 8c shows a time series of the pressure perturbation at a distance of 174 km from the storm, which is in grid 2. Significant distortion of the waves is evident due to their passage into the coarser grid. However, this figure does illustrate the negative pressure lobe of the Lamb wave, which has started to separate from the slower-moving $n1$ mode. Figure 8d shows a time series of the pressure perturbation at a distance of 390 km from the storm, which is in grid 1. Even more distortion of the waves has occurred. Only the Lamb waves generated by the prescribed heating and the latent heat release have reached this location.

In order to illustrate the Lamb wave close to the storm in more detail, an identical simulation was made with

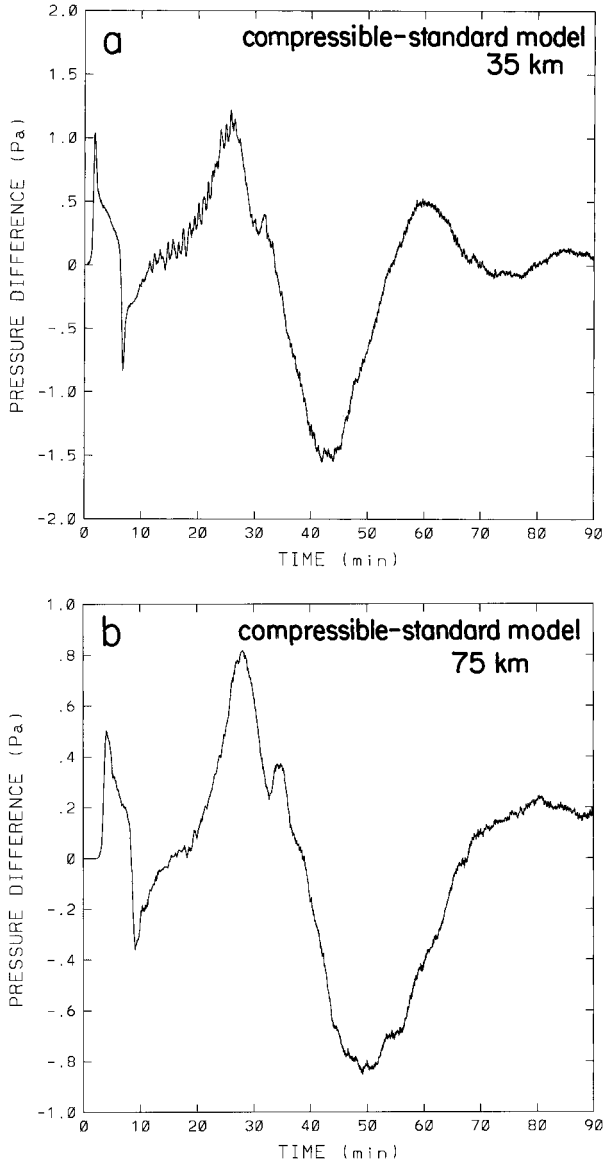

FIG. 9. Difference between the pressure series for the fully compressible and the standard versions of the model for the quiescent case at (a) 35 and (b) 75 km, from the center of the storm.

the standard model discussed in section 4, which does not allow the generation of thermal compression waves. The time series for this run was then subtracted from that for the fully compressible model. It was found that although extremely similar, the storm simulated with the standard model was not identical to the storm simulated with the fully compressible model. Therefore, subtracting the time series does not give the pure compression wave signal since the gravity waves do not have exactly the same amplitudes. The reason for this small difference between the two models is interesting and requires further investigation. Figures 9a and 9b show the difference pressure series between the two model runs at distances of 35 and 75 km from the storm, respectively. In Fig. 9a, the positive peak at $t = 60$ min appears to be due to slightly larger amplitude gravity wave modes in the fully compressible run so that the latter part of this time series needs to be treated with some caution. Nevertheless, it shows much more detail of the Lamb wave close to the storm, in particular the positive lobe and the higher-frequency oscillations, which are superimposed.

This figure can be used to determine the decay rate of the Lamb wave with the horizontal distance traveled from the source. In Fig. 9a, the amplitude of the positive peak of the Lamb wave is 1.23 Pa, which is at a distance of 35 km from the storm. Assuming a $1/(\text{distance})^{1/2}$ decay rate, the amplitude should be 0.84 Pa at 75 km. The simulated amplitude of 0.83 Pa seen in Fig. 9b is in very good agreement with the $1/(\text{distance})^{1/2}$ decay rate.

To determine the decay rate of the $n1$ gravity wave mode generated by the convective storm, we use Figs. 8a and 8b at distances of 35 and 75 km from the storm, respectively, and estimate the contributions to the large trough by the gravity waves produced by the prescribed heating and the Lamb wave. A simulation was run without microphysics with the standard model in order to isolate the gravity waves produced by the prescribed heating. At 35 km from the storm, the contribution to the trough from these gravity waves was found to be -0.4 Pa (not shown) and the contribution from the Lamb wave can be seen to be -1.2 Pa at $t = 39$ min from Fig. 9a. Subtracting these values from the trough amplitude of 14.3 Pa gives an estimate of 12.7 Pa for the amplitude of the $n1$ gravity wave mode, at 35 km from the storm. Assuming a more rapid 1/distance decay rate for gravity waves, then at 75 km the amplitude would be 5.9 Pa. The estimated amplitude of the simulated $n1$ gravity wave mode at this location, using the same procedure as before, is 5.7 Pa. Therefore, the decay rate of the gravity wave with distance traveled is much more rapid than the Lamb wave and appears to be 1/distance. The amplitude of the $n1$ gravity wave mode shown in Fig. 8c, which is in grid 2 at 174 km from the storm, suggests a slightly faster than 1/distance decay rate. The coarse resolution in this grid and weak model diffusion probably account for this faster than predicted decay rate. A 1/distance decay rate is the same as for the three-dimensional solution for a compression wave discussed in section 2. This is perhaps not surprising considering that gravity wave energy propagates upward, not just horizontally like it does for the Lamb wave.

To further investigate the forcing of the waves a bulk method for determining the total latent heat release was formulated. The total accumulated latent heat release can be approximated by

$$\text{LH} = L_c(m_l + P) + (L_c + L_f)m_i, \qquad (9)$$

where m_l is the total mass of liquid water in the domain, m_i is the total mass of ice, P is the accumulated pre-

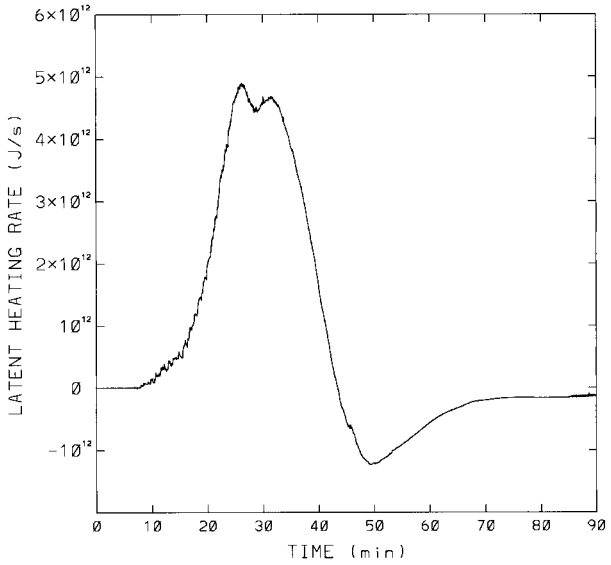

FIG. 10. Total latent heating rate for the quiescent case.

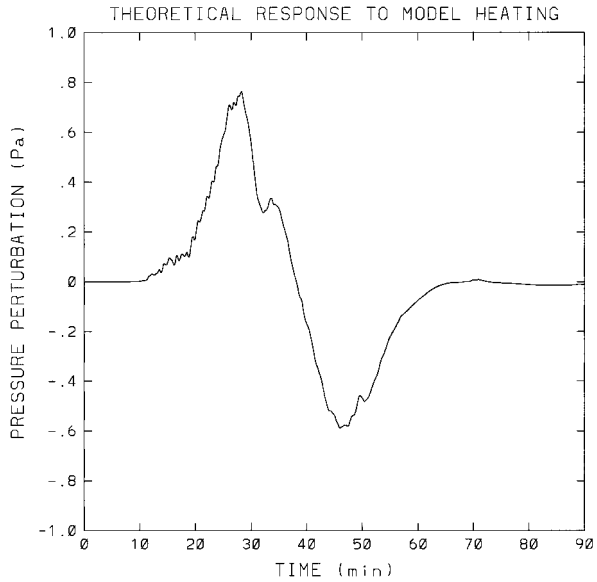

FIG. 11. Results for the idealized two-dimensional linear compression wave model using the same total latent heating rate that occurred in the quiescent case simulation.

cipitation, and L_c and L_f are the latent heats of condensation and fusion taken to be constants of values 2.5×10^6 and 3.34×10^5 J kg^{-1}, respectively. The latent heating rate is the time derivative of LH and is shown in Fig. 10. The first peak occurs at 27 min and is followed shortly afterward by a second smaller peak. The heating rate then rapidly decreases to a negative minimum at 50 min. High-frequency fluctuations are also evident. A closer examination reveals they are particularly large and regular in the growth stage of the convective cell between 11 and 27 min and have a period of approximately 1 min. The high-frequency heating fluctuations have the same period as the high-frequency oscillations seen in the compression wave shown in Fig. 9a and presumably are responsible for forcing them. It is not clear whether they are physical or have a numerical cause. A sensitivity test was carried out reducing the number of small time steps in the time-split scheme to one per long time step and they still occurred. Also, a microphysical iteration procedure was checked for accuracy, but it is possible that other numerical factors could be causing them. On the other hand, high-frequency signals, which have been identified as acoustic in character have been observed to be generated by thunderstorms with similar periods and amplitudes (Bowman and Bedard 1971).

Since the shape of the two-dimensional solution in Fig. 2 is similar to that generated in the numerical model by the prescribed heat source, it is of interest to calculate the idealized two-dimensional solution for the latent heating from the simulated convective storm, shown in Fig. 10. In order to do so, we make use of the fact that the pressure perturbation in a Lamb wave decays with height as $\exp(-z/\gamma H)$, where $H = RT/g$ is the scale height and $\gamma = c_p/c_v$. Although we know that the maximum heating rate is actually elevated above the surface in the simulated rainstorm, we ask what the solution would be if the heating was a maximum at the surface and decayed as $\exp(-z/\gamma H)$. Then we can consider the solution to be a vertical stack of infinitesimal layers with the solution in each layer given by the idealized two-dimensional linear solution and for a heating rate, which decays as $\exp(-z/\gamma H)$. Then the total heating for this idealized scenario is

$$Q_t = \int_0^\infty \int_0^\infty \rho_0 Q_0 \frac{2\pi r b^4}{(r^2 + b^2)^2} \exp(-z/\gamma H)\, dr\, dz, \quad (10)$$

where $r = (x^2 + y^2)^{1/2}$ and $\rho_0 Q_0$ is the heating rate per unit volume at $r = 0$, $z = 0$. Evaluating Eq. (10) gives $Q_0 = Q_t/\gamma H \rho_0 b^2 \pi$. This is the value of Q_0 we use in Eq. (A5) to obtain the pressure perturbation at the surface for the two-dimensional idealized solution, which has the same net heating Q_t as in the simulated storm. The time series for Q_t in Fig. 10 was written out every 1.25 s, which was the model time step. Therefore, the idealized two-dimensional solution for this heating rate was determined by summing up the solutions for a series of pulses spaced 1.25 s apart, for a pulse width of 1.25 s, and for a Q_0, which varies with time as $Q_t(t)/\gamma H \rho_0 b^2 \pi$. This solution is shown in Fig. 11 at a distance of 75 km from the source, which can be compared with the simulated compression wave in Fig. 9b. The amplitude of the positive peak is 0.77 Pa, whereas the amplitude of the simulated positive peak is 0.83 Pa. Given the assumptions used in deriving the idealized two-dimensional solution, the similarity of the amplitude and shape of the wave with the simulated Lamb wave is surprising. The similarity of the amplitudes in particular should be viewed with some caution since it

has been assumed that 1) the atmosphere is isothermal; 2) the heating is maximized at the surface, decreases exponentially with height, and has a horizontal variation give by $Q_0 b^4/(r^2 + b^2)^2$; 3) that all the energy is transferred horizontally by the Lamb waves, that is, that there is no vertical transport; and 4) that latent heating is the primary mechanism for forcing of the Lamb wave, that is, the effects of mass sources and sinks due to phase changes between water and vapor can be neglected. On the other hand, the good agreement could be indicative that the amplitude of the Lamb wave generated is fairly insensitive to the vertical structure of the heating and that only a small fraction of the energy is transferred vertically. The idealized solution shows a smaller second peak, which can also be seen in Fig. 9b. The amplitude of the negative lobe is almost as large as the positive lobe agreeing with Fig. 8d. There are small high-frequency oscillations with the same period as the simulated wave shown close to the storm in Fig. 9a, although their magnitude is quite a bit less. Comparing Figs. 10 and 11 it can be seen that the time it takes for the large positive and negative lobes to pass a location, or the period, is approximately equal to the lifetime of the convective storm. It is recognized that the term ''period'' is being used rather loosely here to refer to the temporal width of this nonrecurrent waveform, as is the term ''frequency'' when referring to the inverse of this period.

Mapes (1993) and McAnelly et al. (1997) have suggested that thermally induced gravity waves may cause uplift of environmental air that could favor the development of additional convection. For this quiescent environment case, the upward displacement at 35 km from the storm was 55 m at 1 h into the simulation. It was centered at 4–5 km above the surface. This appeared to be mainly due to the $n2$ mode with some additional contribution by a higher-order mode or modes. Although not a very large displacement, a number of convective cells in close proximity, or an MCS, might lead to enough uplift to initiate additional convection if the atmosphere is close to being convectively unstable.

A simulation was carried out with the standard model run out to 4 h to examine the longer-term behavior of the gravity waves. Less vertical levels were used, but the horizontal dimensions of grid 3 (grid increment 3 km) were increased to give better resolution of the gravity waves farther from the storm. Figure 12 shows the pressure perturbation series at 174 km from the storm, which is within grid 3 for this simulation. The negative lobe of the $n1$ mode has a minimum of -2.1 mb at 1.4 h, which is a slightly larger amplitude than for the previous simulation with the fully compressible model, which did not have such a good resolution at this location (Fig. 8c). The positive peak of the $n1$ mode, which passes at 1.8 h has clearly separated from the positive peak of the $n2$ mode, which passes at 2.75 h at this location. The $n2$ mode also has a negative lobe with the minimum passing at 3.2 h. In Fig. 8a, at 35 km from the storm, the positive peaks of the $n1$ and $n2$ modes coincide, passing this location at approximately 59 min, although it is difficult to say from this figure at exactly what time each mode passes. Therefore, the estimated speed of the $n2$ mode calculated from the times its positive peak passes 35 km (Fig. 8a) and 174 km (Fig. 12) is 139 km divided by 106 min giving 22 m s^{-1}, which is slightly less than half the speed of the $n1$ mode, which propagates at approximately 48 m s^{-1}. Estimating the speed of the $n2$ gravity wave mode from another time series written out during the long duration run, when the $n2$ peak was clearly visible, gave a speed of 23 m s^{-1}.

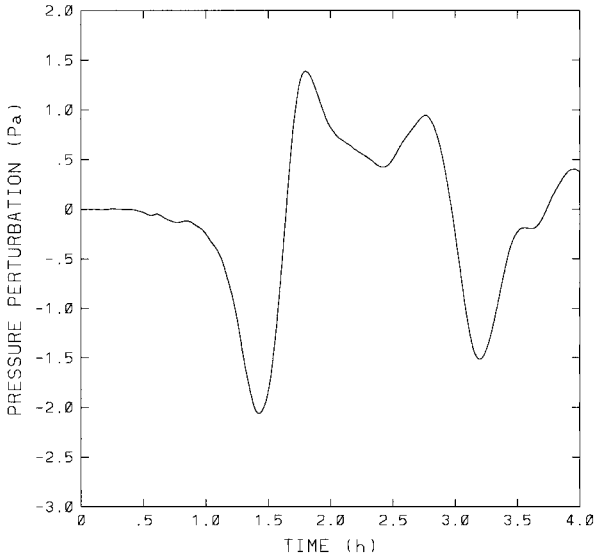

FIG. 12. Time series of the pressure perturbation series for a longer duration simulation of the quiescent case using the standard version of RAMS, at 174 km from the center of the thunderstorm.

b. Vertical wind shear case

Figure 13 shows a vertical cross section of the condensate and wind vectors at 40 min for the shear case. The updraft tilts downshear with strongest velocities on the upshear side of the storm. At upper levels, the condensate is advected downstream forming an anvil. The maximum value of the condensate mixing ratio is slightly less at this time than for the quiescent case. The strongest updrafts occurred around 30 min, at $z = 10$ km, and the peak value was 32 m s^{-1}. This was a longer-lived storm than the quiescent case with a significant updraft at 90 min. The precipitation maximum was 75 mm. The rainfall also occurred over a larger area than for the quiescent case and the total was twice as much.

Figure 14 shows a horizontal cross section of the wind vectors and pressure perturbation 200 m above the surface at 60 min. The high pressure perturbation region >18 Pa in the center of the figure is approximately the area occupied by the cold pool outflow. The low pres-

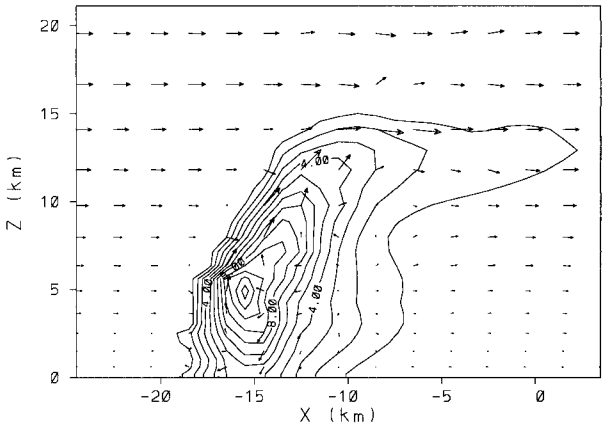

FIG. 13. Vertical cross section of the total liquid and ice hydrometeor mixing ratio and wind vectors for the shear case, at 40 min. The contour interval is 1 g kg^{-1} and the maximum wind vector is 30 m s^{-1}.

sure anomaly associated with the $n1$ gravity wave mode can be seen exiting the west, south, and north boundaries of the fine grid. It has already exited the east boundary since the mean wind in the troposphere is $\sim$8 m s^{-1} toward the east. There is an asymmetry of the high pressure anomaly with fairly large values extending north and south of the storm.

Figures 15a and 15b show vertical cross sections of the pressure perturbation and temperature perturbation, respectively, at 65 min in grid 4. There is a distinctive $n2$ looking structure between $x = -30$ km and $x = -45$ km. This consists of warm air at upper levels with cool air beneath and the characteristic high/low/high pressure

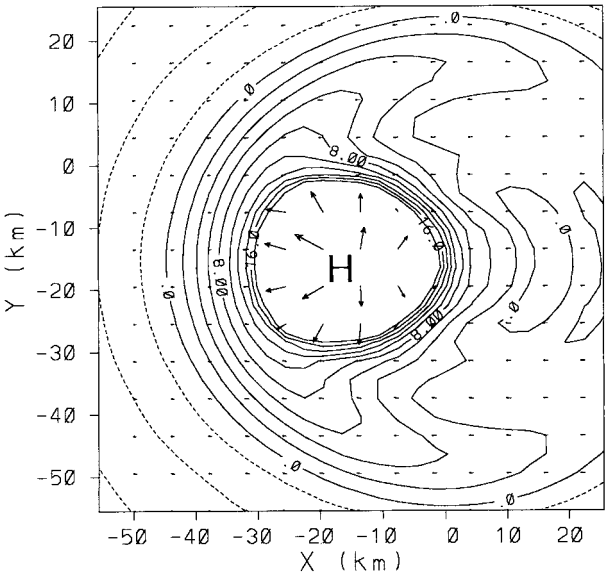

FIG. 14. Horizontal cross section of the wind vectors and pressure perturbation 200 m above the surface for the shear case, at 60 min. The maximum wind vector is 14 m s^{-1} and the contour interval is 2 Pa. Here H indicates pressure perturbations higher than 18 Pa.

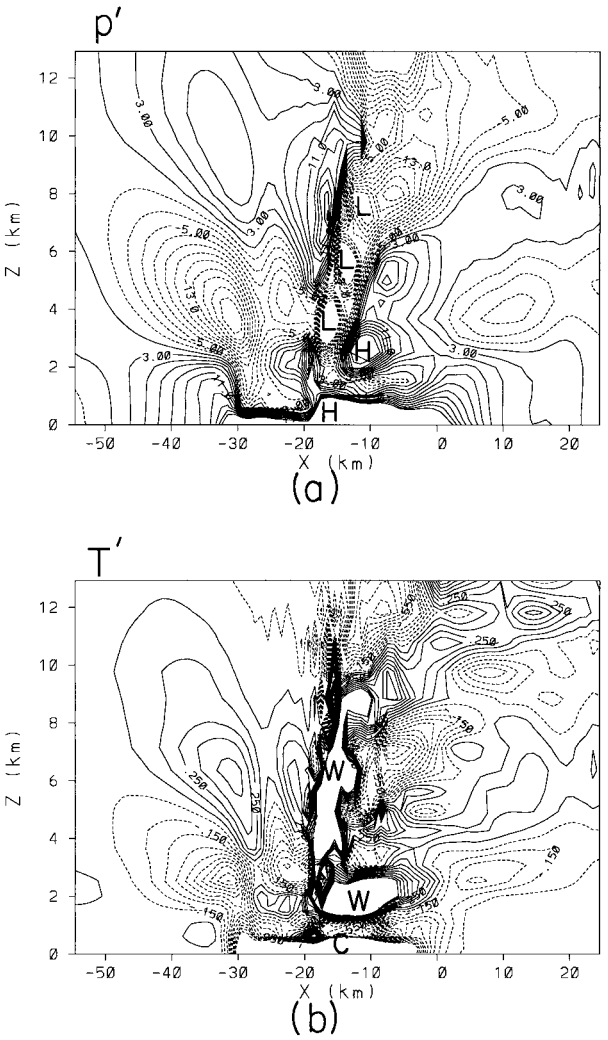

FIG. 15. Vertical cross sections for the shear case at 65 min. (a) The pressure perturbation p'. The contour interval is 2 Pa. Here H and L indicate pressure perturbations higher than 21 Pa and lower than -21 Pa, respectively. (b) The temperature perturbation T'. The contour interval is 0.1 K. Here W and C indicate temperature perturbations greater than 1 K and less than -1 K, respectively.

perturbations. Since the environment is near dry adiabatic between the surface and 1.5 km, the pressure perturbations associated with the gravity waves are nearly constant with height in this layer and the temperature perturbations are small. The cold pool has a temperature deficit of $\sim$2.5 K and is formed by evaporatively cooled air sinking and spreading out at the surface. Velocities are strong in the cold pool at this time, so nonlinear advective effects are important, whereas the gravity wave modes are much more linear in character.

Figures 16a–c show time series of the pressure perturbation 35 km to the west, 35 km to the east, and 390 km to the west of where the storm was initiated, respectively. The Lamb wave generated by latent heat release is not very evident 35 km from the storm. The

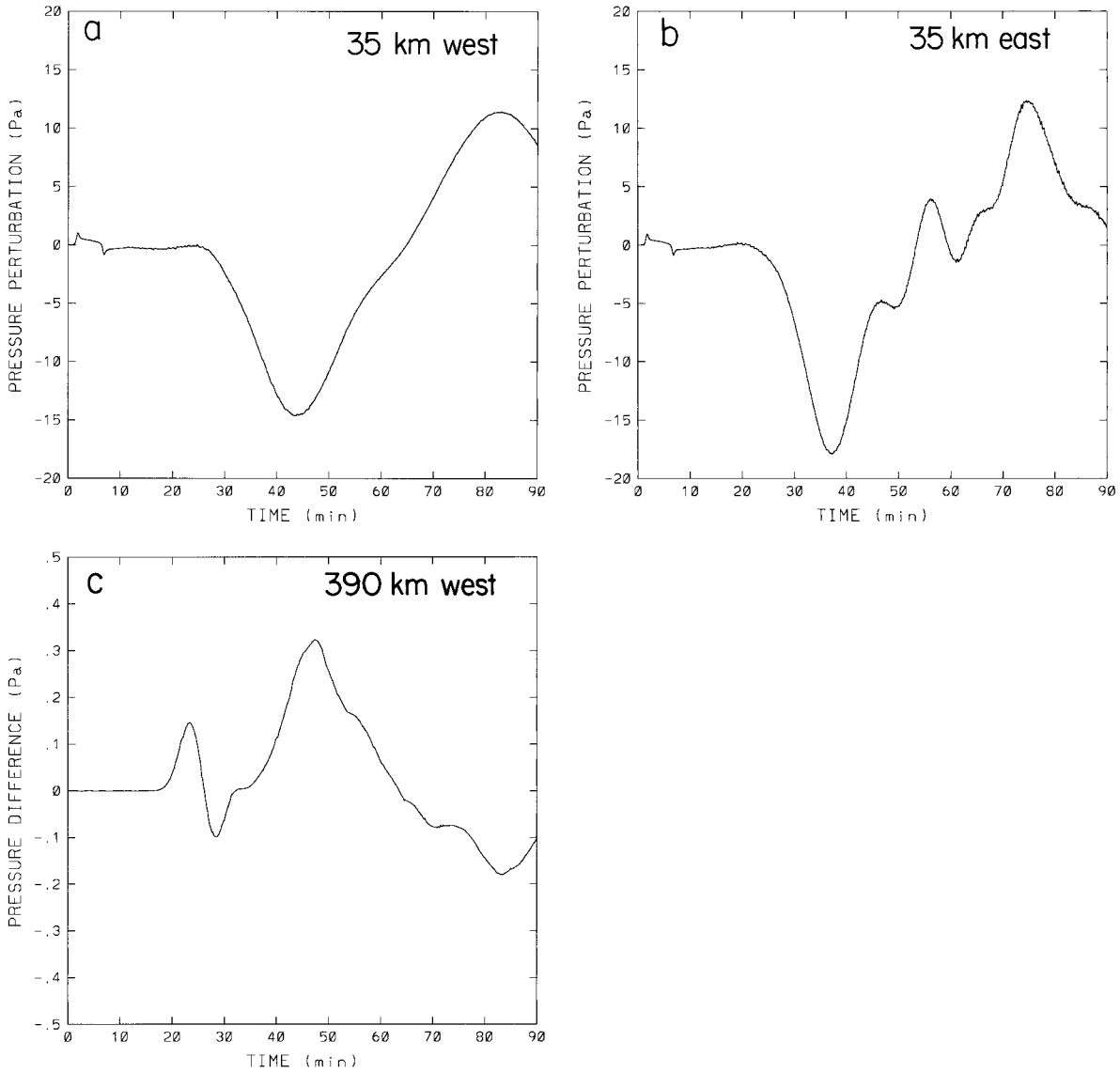

FIG. 16. Time series of the pressure perturbation near the surface for the shear case at (a) 35 km to the west, (b) 35 km to the east, and (c) 390 km to the west of where the thunderstorm was initiated.

*n*1 gravity wave mode can be clearly identified in both Figs. 16a and 16b. On the east side of the storm, the time it takes for the negative lobe of the *n*1 mode to pass is less, mainly because the mean westerlies cause the wave to pass this location more quickly. However, the instantaneous fields show that the *n*1 mode does appear to be broader and slightly weaker in amplitude east of the storm. Also, the high pressure maxima aloft is more elevated than on the west side of the storm. The high pressure peak at 83 min in Fig. 16a seems to be due to a superposition of the positive lobes of the *n*1, *n*2, and *n*3 modes. On the east side of the storm, the high pressure peak at 57 min appears to be due to a weak *n*2 structure, while the stronger peak at 75 min appears to be an *n*3 structure. The effects of shear on the modes, especially on the slower-moving higher-order ones, are obviously quite complicated. However, these results do show how different the waves observed at locations upshear and downshear of storms are likely to be. It can be inferred that the compression wave seen in Fig. 16c has a longer wavelength than for the quiescent case (Fig. 8d). The interval between the positive and negative peaks is 37 min, whereas for the quiescent case it is only 20 min. The magnitude of the negative peak is less than for the quiescent case. Figure 17 shows the total latent heating rate. Comparing with Fig. 10 for the quiescent case, it can be seen that the maximum occurs a bit later and is a bit larger. There is far more net heating for the shear case. As a result of the convection being long lived, the net heating does not be-

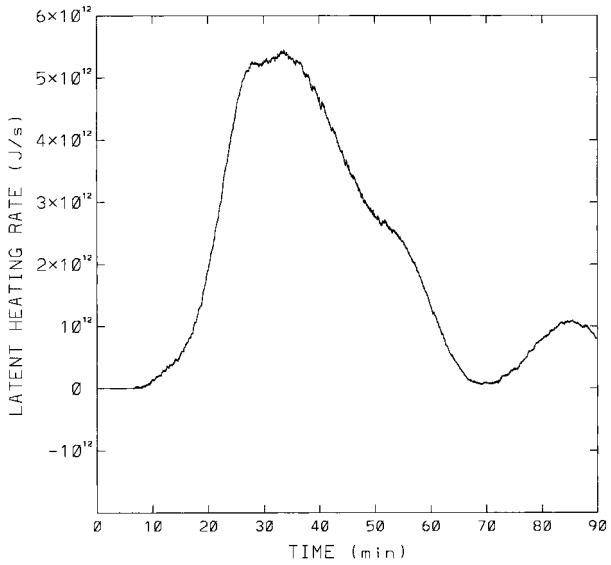

FIG. 17. Total latent heating rate for the shear case.

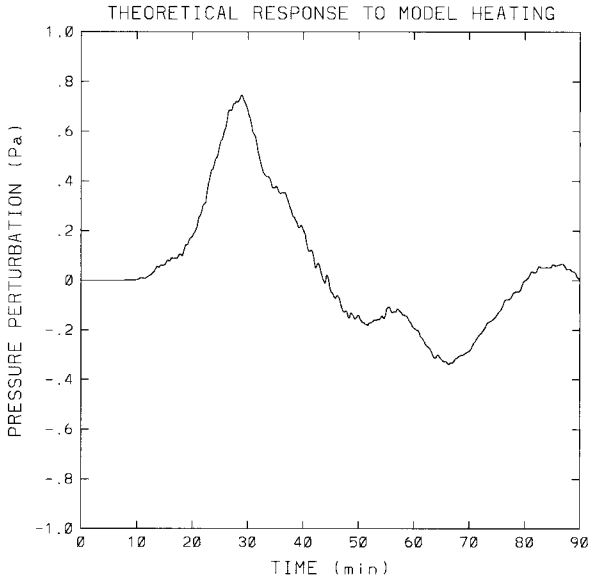

FIG. 18. Results for the idealized two-dimensional compression wave model using the same total latent heating rate that occurred in the shear case simulation.

come negative unlike the quiescent case. Figure 18 shows the idealized two-dimensional linear solution for this heating rate at 75 km from the storm. This is very similar in structure to the simulated compression wave shown in Fig. 16c. The peak value is almost the same as for the quiescent case and occurs at almost the same time. The peak value does not correlate well with the peak heating rate in Fig. 15, but leads it by about 8 min after taking into account the time taken for the wave to travel 75 km. This is a consequence of the amplitudes of the wave depending on the rate of change of the heating rate, not just its magnitude.

c. *Transfer of internal and gravitational potential energies*

NPa and NPb discussed how compression waves could transfer total energy in the atmosphere at the speed of sound. The total energy flux vector appearing in the total energy equation is given by $E_t\mathbf{u} + p\mathbf{u}$ where E_t is the total energy $\rho(c_vT + gz + u^2/2)$, $E_t\mathbf{u}$ is the flux of total energy carried by the flow itself, and $p\mathbf{u}$ is the pressure work term [see, e.g., Gill 1982, his Eq. (4.74); NPA, their Eq. (4)], where for simplicity radiation effects and diffusion of heat and kinetic energy have been neglected. Since the energy flux vector is not simply $E_t\mathbf{u}$, but includes the pressure work term $p\mathbf{u}$, there is not such a simple interpretation of total energy transfer as there is, for instance, for mass transfer, where the rate of change of mass in a volume depends just on the mass fluxes $\rho\mathbf{u}$ across the surface of the volume. Nevertheless, due to the conservative form of the total energy equation, perturbations of total energy field can be seen to move around from one region to another with total energy being conserved, as seen in the analytical and numerical model examples presented in NPa. It is in this sense that we refer to total energy transfer. This situation is by no means unique. For ordinary sound waves and internal gravity waves the wave energy flux vector is not $E_w\mathbf{u}$, where E_w is the wave energy [see, e.g., Gill 1982, his Eq. (6.14.7); NPa, their Eqs. (21) and (36)]. Yet it is common to refer to wave energy as being transferred by these types of waves, with the understanding that the transfer is not due to the flux $E_w\mathbf{u}$ but to the wave energy flux vector.

In NPa the internal energy per unit volume $E_i = \rho c_vT$ was rewritten using the equation of state $p = \rho RT$ for a dry atmosphere as c_vp/R. Internal energy perturbations c_vp'/R from an initial internal energy $c_vp_0(z)/R$ were considered. This perturbation form should not be confused with the perturbation energy, or wave energy, mentioned in the introduction, which involves linear approximations. It is simply the difference after subtracting the large amount of internal energy present in the initial state and does not involve any approximations [see Eq. (7) of NPa, and sections 4 and 5 of that paper for discussion of wave energy]. Looking at Fig. 1b, the two-dimensional solution for p', at a particular location versus time for the linear compression wave model, it may not be obvious that this wave results in a net transfer of internal energy, since it has a negative lobe as well as a positive lobe. Figure 19 shows the pressure perturbation and internal energy perturbation versus distance from the source for the same wave. Since this is a cylindrical wave, the energy per unit length in an increment of radius dr is $2\pi rc_vp'\,dr/R$. The internal energy per unit area $2\pi rc_vp'/R$, plotted in this figure, shows that the factor $2\pi r$ leads to an increase in the

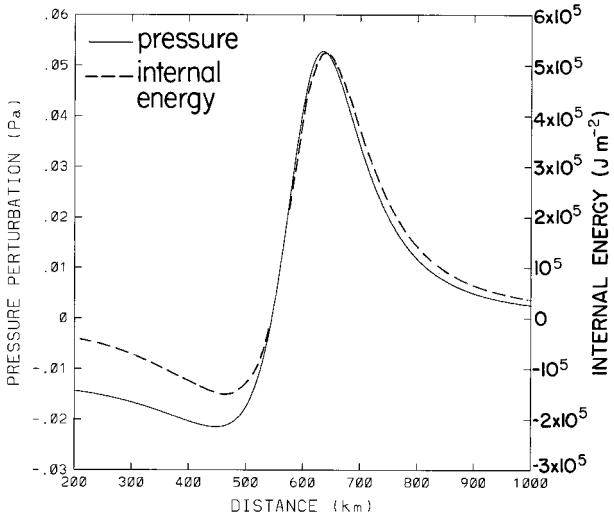

FIG. 19. Pressure perturbation (solid line) and internal energy perturbation (dash line) plotted as a function of distance from the source for the two-dimensional linear compression wave model.

positive area beneath the curve and a decrease in the negative area compared to the curve for p', which results in a net positive internal energy in the wave. For this linear model, the net energy input is exactly equal to the net internal energy. There is also some kinetic energy associated with the wave so that the total energy does not add up to exactly equal the net energy input. This small error is a result of linearizing the equations as discussed in NPa.

For the numerical convective storm simulation, the effects of moisture need to be included. Using the equation of state $p = \rho RT(1 + 0.61w)$, the internal energy perturbation to a good approximation is

$$E_i' = \frac{c_v p}{R(1 + 0.61w)} - \frac{c_v p_0}{R(1 + 0.61w_0)}. \quad (11)$$

Since the resolution in the coarser grids for the three-dimensional simulation is not very good and results in a distortion of the waves, an energy analysis was also carried out for a two-dimensional simulation with a much better coarse-grid resolution (3-km grid increment). The energies were calculated from the surface to 50 km, so as not to include the upper-level Rayleigh friction layer. The gravitational potential energy perturbation per unit volume was calculated as $\rho' gz$. For this simulation, it was found that the sum of the perturbation internal and gravitational potential energies within the domain was 87% of the latent heat released in the domain calculated according to Eq. (9). This disagreement is mainly due to the loss of mass from the air due to phase changes from vapor to liquid and ice water. This conclusion is supported by a simulation with the mass source term S in Eq. (8) eliminated, which resulted in a very good agreement between the sum of the perturbation internal and gravitational potential energies in the domain and the latent heat release. The loss of water vapor from the air as condensation occurs, represented by a negative value of S in Eq. (8), opposes to some extent the expansion brought about by latent heat release resulting in slightly weaker amplitude Lamb waves than would otherwise occur. After the convection has almost completely dissipated and the two oppositely moving Lamb waves had separated from the slower moving gravity waves, the energies were calculated separately for the two outer regions occupied by the Lamb waves and the central region occupied by the gravity waves. Since there were still cloud remnants, there were some very small compression wave perturbations within the region occupied by gravity waves. In the Lamb wave regions, the ratio of perturbation gravitational potential energy to perturbation internal energy was 0.4. This ratio is the well-known proportion R/c_v of gravitational to internal energy for a hydrostatic atmosphere (see, e.g., Holton 1979). The sum of these energies in the Lamb wave regions was slightly greater than the total in the domain and equal to 88% of the total latent heat release. In the region occupied by gravity waves, the net perturbation gravitational potential energy was negative. Its magnitude was ~2% of the total latent heat release. This decrease is predominantly due to a net decrease in density in this region due to expansion of air brought about by the latent heat release. The net perturbation internal energy in this region was positive with a magnitude of ~1% of the latent heat release. This small increase is apparently due to a reduction of the net moisture in this region brought about by precipitation, which tends to increase the first term of Eq. (11) relative to the second term. An energy analysis for the three-dimensional simulation shows similar results, although the poorer resolution in the coarser grids was probably responsible for a larger difference between the net latent heat release and the net energy perturbation. The net kinetic energy within the domain reached a maximum during the growing phase of the convective cell and was approximately 1% of the total change in internal and gravitational potential energies that had occurred. To check the three-dimensional results an idealized simulation was run with fewer vertical levels, but with better horizontal resolution in the coarse grid. Convective heat release was represented by a large magnitude prescribed heat source and the microphysical scheme was not implemented. Good energy conservation was obtained and the Lamb wave was clearly transferring internal energy and gravitational potential energy to the periphery of the domain at the speed of sound.

d. Resurgence of convection

For the longer duration quiescent case simulation, an interesting small-scale buoyancy oscillation occurred at low levels after the storm decayed. Figures 20a–c show vertical cross sections of the temperature perturbation, water vapor mixing ratio perturbation, and the x component of velocity, respectively, at 90 min. There is a

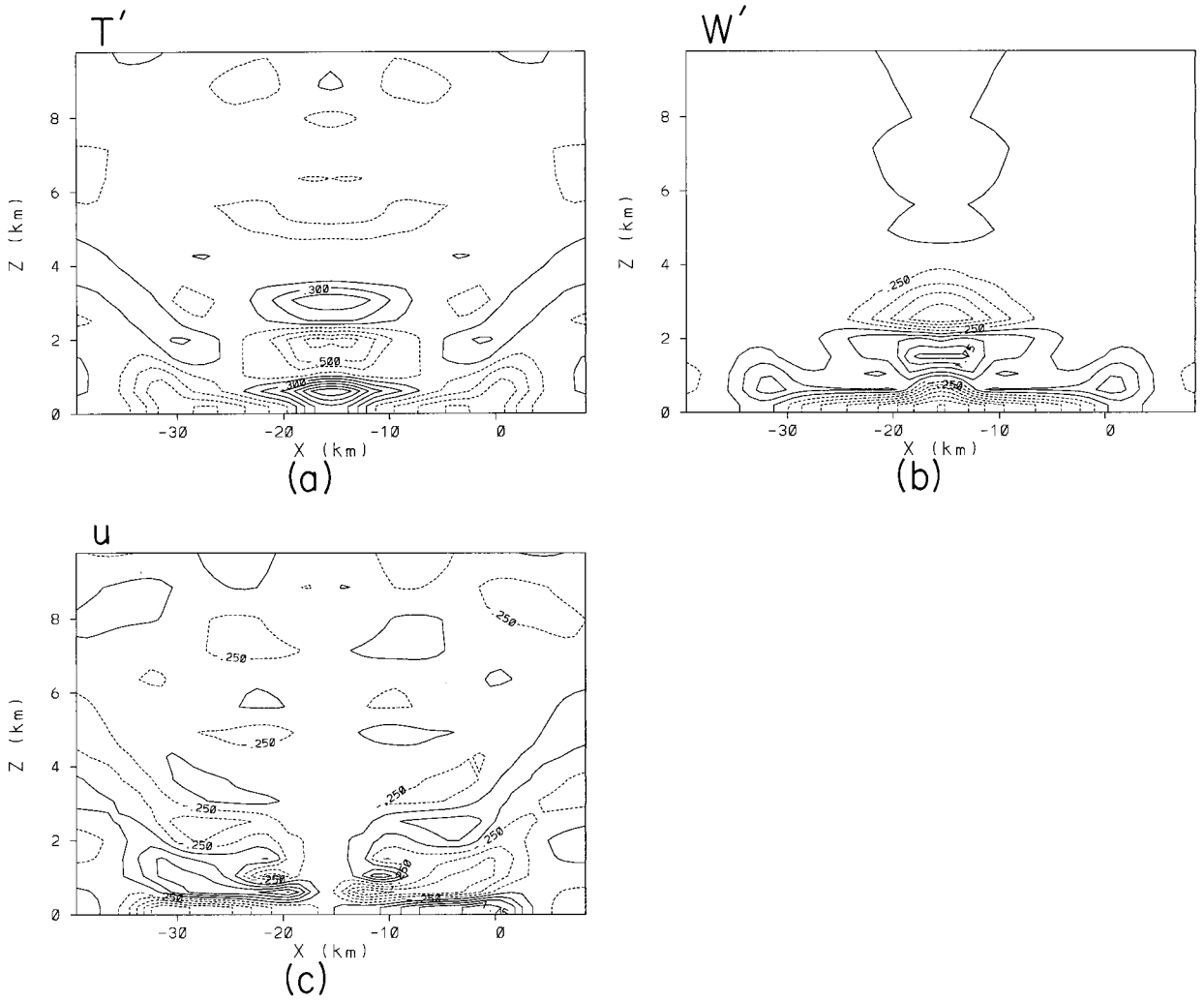

FIG. 20. Vertical cross sections for the quiescent case at 90 min. (a) Temperature perturbation T'. The contour interval is 0.2 K. (b) Water vapor mixing ratio perturbation w'. The contour interval is 0.5 g kg^{-1}. (c) The x component of velocity u. The contour interval is 0.5 m s^{-1}.

warm bubble of air next to the surface caused by the downdraft air overshooting its equilibrium level. The maximum temperature anomaly in the bubble is 1.1 K. It is centered in the middle of the cold pool outflow, which at this time is only 0.7 K colder than the environment near the surface. The downdraft air was much drier than the environmental air near the surface and has resulted in a moisture deficit of approximately 3 g kg^{-1}. As the cold pool spread out at the surface, the vertical motion at the leading edge lifted up the moist environmental air that was then advected back over the cold pool. This is partly responsible for the large moisture anomaly above the warm bubble of $\sim$2 g kg^{-1}. This moisture anomaly also resulted from moist air, which was advected toward the storm at low levels early on and lifted up, but did not make it into the main updraft. When the downdraft formed, it brought dry air through the center of this moist region. As the downdraft weakened, horizontal and vertical advection of the moist surrounding air led to the formation of the large moisture anomaly in the region that had been occupied by the downdraft. The horizontal velocity field shows quite strong horizontal convergence within the warm bubble as the air starts to rebound. The ensuing upward motion in the moist anomaly caused a small cloud to form at 110 min. Figure 21 shows the total liquid and ice mixing ratio at 130 min, which is 40 min after the rebound started to occur. A narrow convective cell with a maximum mixing ratio of 6 g kg^{-1} has formed. This develops into a storm similar to the first, but less intense, with approximately two-fifths of the heat release. The time lag between the peak heating rates for the two storms was 1 h and 50 min. Apparently, the moisture that had advected over the top of the first storms cold pool was a major source of convective available potential energy (CAPE) for the second storm.

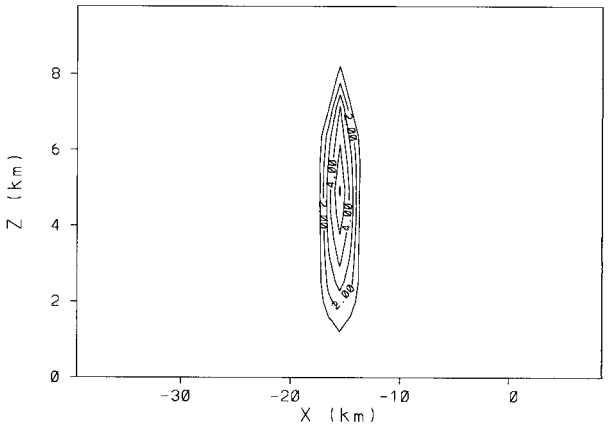

FIG. 21. Vertical cross section of the total liquid and ice mixing ratio for the quiescent case at 130 min. The contour interval is 1 g kg^{-1}.

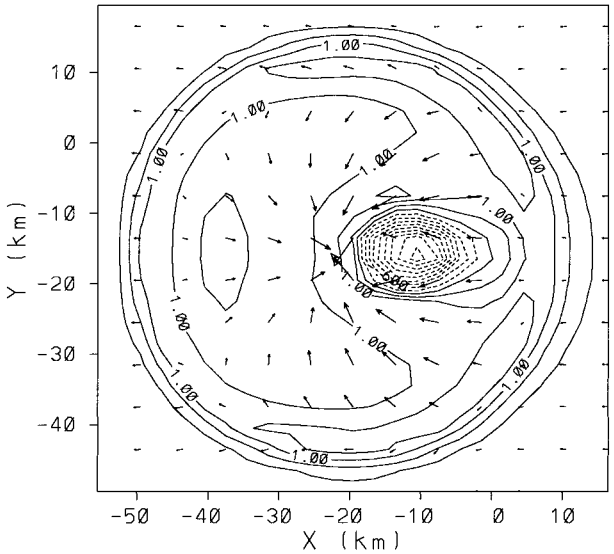

FIG. 22. Horizontal cross section of the wind vectors and water vapor perturbation for the shear case 600 m above the surface at 120 min. The contour interval is 0.4 g kg^{-1}.

It is possible that this mechanism may sometimes play a role in resurgences of convection in nature. McAnelly et al. (1997) discussed two mesoscale convective systems that exhibited an early meso-β-scale convective cycle (a maximum and subsequent minimum) followed by reintensification. In that paper, it is suggested that the $n2$ gravity wave mode has the effect of modifying the environment for convection and hence may play a role in the reintensification and upscale growth of convection. It is also possible that the small-scale low-level buoyancy oscillations found in this study could sometimes play a role by initiating new convection in MCSs, along with other low-level forcing mechanisms such as gust fronts, and that some of the CAPE for the reintensification may come from the moist air atop the cold pools from the earlier convection.

The first cell, which developed in the shear case was longer lived than for the quiescent case, as can be seen from comparing the latent heating rates in Figs. 10 and 17. The initial strongest cell for the quiescent case decayed almost completely because of the development of the downdraft, caused by waterloading and evaporation, which very effectively cut off the low-level updraft circulation. Due to the updraft tilt that occurred for the shear case, the downdraft formed on the downshear side of the updraft, so that the updraft circulation was maintained longer. However, as can be seen in Fig. 17, the net latent heating was reduced to near zero by 67 min. This came about because of the development of a deep cold pool at 60 min, which blocked the flow of low-level air into the updraft. Also, because some of the cold dry downdraft air, which formed the cold pool was entrained into the updraft from the downshear side. The updraft did not completely disappear, however, but managed to maintain itself by feeding on moist environmental air, which had been advected over the cold pool. Although a warm bubble formed near the surface on the downshear side when the downdraft overshot its buoyant equilibrium level, there was not a rebound producing a resurgence of convection. This occurred because the downdraft was continually maintained in this region since the storm did not completely decay. Therefore, the warm bubble was under a rain shaft and drier air from aloft was maintained over it. The storm remained weak for almost an hour, after which a moderate resurgence to a quasi-steady state occurred. This resurgence coincided with the cold pool becoming more shallow. This apparently reduced the low-level blocking of inflow and the entrainment of cold dry air near the surface into the updraft. The storm regained moderate strength by feeding on the moist air atop the cold pool. Figure 22 shows the wind vectors and water vapor perturbation 600 m above the surface at 120 min, which is the time the resurgence took place. As can be seen, the updraft is feeding on moist air, approximately 1 g kg^{-1} moister than the environment, from all sides of the storm, except immediately downshear, which is the very dry downdraft region.

Gravity waves were produced by these resurgences of convection for both cases, but none as strong as those produced by the initial cells. It is possible that the $n1$ mode induced during the quasi-steady stage for the shear case may have had a role in enhancing the low-level flow of moist air atop the cold pool, contributing to the longevity of the storm. During this stage, the updraft continually built on the upshear side and was often quite vertical at low levels, whereas at upper levels it tilted downshear. The hydrometeors were then advected downstream at upper levels maintaining the anvil. In this quasi-steady stage the storm did not move with the mean flow in the troposphere, but was approximately stationary with respect to the environmental air in the lowest kilometer.

6. Discussion and conclusions

Results of the linear model of a thermally induced compression wave and the numerical simulations with a fully compressible cloud model show that a low-frequency thermal compression wave is generated by a convective storm, which is a Lamb wave that decays with 1/(distance)$^{1/2}$. A positive heat source generates a wave with both positive and negative lobes. Results of the cloud model indicate that the peak-to-trough amplitude of the Lamb wave at 75 km from an isolated thunderstorm is likely to be about 1.5 Pa. When the latent heat release generated in the numerical convective storm simulations were used in the linear idealized model it produced very similar looking compression waves as were simulated for both the quiescent and shear cases. This confirms that the low-frequency thermally induced compression waves produced by the cloud model have properties of two-dimensionally propagating waves. Also, the idealized linear model may be useful for determining the horizontal structure and amplitude of thermal compression waves produced in more complicated convective situations, if the latent heat release is known. For instance, hurricanes, for which estimates of latent heating rates could be readily obtained from numerical simulations, but for which there would be boundary condition problems to overcome before a fully compressible model could be used to determine the compression wave signature.

Since the speed of the low-frequency compression waves depends on (temperature)$^{1/2}$, and they do not interact with convection, they are able to propagate through storms without much impediment. Also, since they are deep disturbances, they are unlikely to be greatly modified by topography.

High-frequency components to the signal occurred in the simulated waves, which have similar periods and amplitudes as those observed by Bowman and Bedard (1971). At this stage, it is not possible to conclusively state that the higher-frequency components do not have some numerical source but their consistency with observations is encouraging. Some preliminary high-resolution two-dimensional simulations indicate that very high-frequency components are likely to be damped with horizontal distance traveled due to the variation of the speed of sound with height caused by temperature changes and also to relative changes in the propagation speed caused by wind shear. This is because for a very short wavelength, the upper-level disturbance does not have to move very far relative to the low-level disturbance before resulting in a large hydrostatic reduction of the surface pressure.

For the quiescent case, it was easy to identify distinct thermally induced gravity wave modes. The $n1$ mode propagated at $\approx$48 m s^{-1} and the pressure perturbation at the surface had both a positive and a negative lobe. The $n2$ mode propagated at approximately half the speed and had a positive lobe followed by a negative lobe at the surface. Higher order modes were also evident. The gravity wave modes decayed as 1/distance; a much more rapid rate than for the Lamb wave. This is the same decay rate as for three-dimensionally propagating waves indicating a large vertical transport of wave energy, which could play an important role in the dynamics of the middle atmosphere (Alexander et al. 1995). The vertical uplift produced by the gravity wave modes for the quiescent case was 55 m, at 35 km from the storm. Although, not very large, it is possible that a number of convective cells acting together could produce enough uplift to initiate new convection, or enhance preexisting convection in some situations. In two-dimensional simulations that have been carried out, the gravity waves decay with the slower rate of 1/(distance)$^{1/2}$ so that for linearly organized convective systems the perturbations produced by the gravity wave modes would be significantly larger. The $n1$ mode was easy to distinguish in the shear case, but the effect of wind shear made it difficult to clearly identify the higher-order modes and how they were behaving. There was a pronounced asymmetry, with a large amplitude $n2$ looking structure on the upshear side of the storm, but not on the downshear side. This could play a role in the upper-level blocking of the flow causing it to diverge round the storm.

An energy analysis showed that the amount of internal energy and gravitational potential energy transferred by the Lamb wave was approximately equal to the net increase of total energy brought about by the convective storm. This result supports the theory put forward by NPa and NPb that total energy can be transferred very effectively at the speed of sound by compression waves and is not simply an advected quantity, which has been the view of many large-scale observational studies.

The mechanisms for decay and resurgence of convection discussed in section 5d may sometimes be responsible or contribute to the early meso-β convective cycle that has been observed in many MCS's (McAnelly and Cotton 1992; McAnelly et al. 1997). Cold pools are often thought to be detrimental to convection when they flow beneath an updraft, since CAPE for the storm is reduced. The results of this study suggest that although true, certainly in the short term, it is possible for convection to redevelop by feeding on moist environmental air that has flowed over the cold pool. This could be a significant source of CAPE for some MCSs aiding in their long-term development.

It is hoped that the results of this study will aid in detecting and recognizing thermally induced compression waves and gravity waves. Signal processing techniques similar to those employed by Einaudi et al. (1989) could be designed specifically to detect these waves. The thermally induced gravity waves produced by an isolated thunderstorm could be detected using pressure sensors with a resolution of about 1 Pa. Correlation of signals at different locations would be necessary to clearly distinguish the part of the signal as-

sociated with each particular gravity wave mode. The amplitude of the signal decreases as 1/distance, which could be used to help correlate signals at different locations. Using arrays of sensors at different locations, signal processing could be used to determine the direction of the source and triangulation applied to determine the position of the source.

Thermally induced compression waves are far harder to detect, since they are small amplitude waves that are likely to be superimposed with larger amplitude thermally induced gravity waves, as well as disturbances produced by other sources. However, their much faster propagation speed could be used to correlate signals at different locations in order to extract the part of the pressure signal due to them. For an isolated thunderstorm the resolution of a pressure sensor would need to be about 0.1 Pa. The existence of these waves could probably be verified relatively easily by using a triangular array of sensors spaced approximately 10 km apart (A. J. Bedard 1998, personal communication). Compression waves could be distinguished from gravity waves since they would appear almost simultaneously across the array, whereas for gravity waves there would be noticeable delays. A wave from an isolated thunderstorm would be of small amplitude and hard to detect. The best chance would be for multiple sources of convection, which develop at the same time, or for a rapidly developing MCS. A continuously operating sensor array might be in a favorable location at times relative to multiple sources, to detect a large superimposed signal, or a large amplitude compression wave produced by a MCS.

Latent heating and cooling are the main mechanisms for generating the compression waves in this study, but density changes due to moisture sources and sinks have been shown to have significant effects, which deserve further examination. Thermally induced compression waves are also generated by solar heating and therefore they could have some relevance for solar tides. Shaffer et al. (1997) included thermal-induced compression waves as one of the possible mechanisms for what appears to be a lunar-induced temperature modulation of the polar regions. Future investigations could utilize fully compressible global models to examine if thermally induced compression waves have any significant large-scale effects.

Acknowledgments. Discussions with Dr. Alfred Bedard concerning possible methods of observing compression waves were most helpful. This research was supported by Colorado State University's Geosciences Program, Grant DAAL0198-2-0078. We particularly thank Ken Eis and Dr. Thomas Vonder Haar. Discussions with Dr. Robert Walko and Dr. Jason Nachamkin are appreciated. Thanks to Dallas McDonald and Tara Pielke for preparing this manuscript.

APPENDIX

Solution for the Linear Model

The two-dimensional solution to Eq. (4) is obtained by first finding the three-dimensional solution for the heat source $Q_m = P(t)Q_0 b^4/(r^2 + b^2)^2$, and then considering the compression wave produced by an infinite line of sources of heating (see, e.g., Lighthill 1978). In spherical coordinates, Eq. (4) becomes

$$\frac{\partial^2 \zeta}{\partial t^2} - c^2 \frac{\partial^2 \zeta}{\partial r^2} = \alpha \frac{\partial}{\partial t}(rQ_m), \tag{A1}$$

where $\zeta = rp'$ and $\alpha = c^2\rho_0/c_pT_0$. Taking Laplace and Fourier transforms we find,

$$\hat{\tilde{\zeta}} = \alpha(\widetilde{rQ_m}) \frac{s}{(s^2 + c^2k^2)} e^{-as} \frac{(1 - e^{\epsilon s})}{s}, \tag{A2}$$

where (^) represents both the Laplace and Fourier transformed variable and (~) just the Fourier transform. Here s and k are the parameters associated with the Laplace and Fourier transforms, respectively. Taking the inverse transforms gives

$$p'_{3D} = \frac{c\rho_0 b^4 Q_0}{c_p T_0} \left\{ \frac{c(a + \epsilon - t)}{\{[r + c(a + \epsilon - t)]^2 + b^2\}\{[r - c(a + \epsilon - t)]^2 + b^2\}} + \frac{c(t - a)}{\{[r + c(t - a)]^2 + b^2\}\{[r - c(t - a)]^2 + b^2\}} \right\}. \tag{A3}$$

The two-dimensional solution is obtained by integrating along a line of three-dimensional sources located along the z axis,

$$p'_{2D} = \frac{1}{b\pi} \int_{-\infty}^{\infty} p'_{3D}(r - ct, r + ct)\, dz, \tag{A4}$$

where $1/b\pi$ is a factor to convert to a heating rate of $Q_0P(t)b^4/(x^2 + y^2 + b^2)$ per unit length along the line. If s is the perpendicular distance from a point at $z = 0$ to the line, then $r = (s^2 + z^2)^{1/2}$, so that the solution can be written

$$p'_{2D} = \frac{2c\rho_0 b^4 Q_0}{b\pi c_p T_0} \int_0^\infty \left\{ \frac{c(a + \epsilon - t)}{\{[\sqrt{s^2 + z^2} + c(a + \epsilon - t)]^2 + b^2\}\{[\sqrt{s^2 + z^2} - c(a + \epsilon - t)]^2 + b^2\}} + \frac{c(t - a)}{\{[\sqrt{s^2 + z^2} + c(t - a)] + b^2\}\{[\sqrt{s^2 + z^2} - c(t - a)]^2 + b^2\}} \right\} dz. \quad \text{(A5)}$$

This integral is evaluated numerically.

REFERENCES

Alexander, M. J., J. R. Holton, and D. R. Durran, 1995: The gravity wave response above deep convection in a squall line simulation. *J. Atmos. Sci.,* **52,** 2212–2226.

Bannon, P. R., 1995: Hydrostatic adjustment: Lamb's problem. *J. Atmos. Sci.,* **52,** 1743–1752.

——, 1996: Nonlinear hydrostatic adjustment. *J. Atmos. Sci.,* **53,** 3606–3617.

Bowman, H. S., and A. J. Bedard, 1971: Observations of infrasound and subsonic disturbances related to severe weather. *Geophys. J. Roy. Astr. Soc.,* **26,** 215–242.

Bretherton, C. S., and P. K. Smolarkiewicz, 1989: Gravity waves, compensating subsidence and detrainment around cumulus clouds. *J. Atmos. Sci.,* **46,** 740–759.

Eckart, C., 1960: *Hydrodynamics of Oceans and Atmospheres.* Pergamon Press, 290 pp.

Einaudi, R., A. J. Bedard Jr., and J. J. Finnigan, 1989: A climatology of gravity waves and other coherent disturbances at the Boulder Atmospheric Observatory during March–April 1984. *J. Atmos. Sci.,* **46,** 303–329.

Gill, A. E., 1982: *Atmosphere–Ocean Dynamics.* International Geophysics Series, Vol. 30, Academic Press, 662 pp.

Holton, J. R., 1979: *An Introduction to Dynamic Meteorology.* International Geophysics Series, Vol. 23, Academic Press, 391 pp.

Johnson, R. H., B. D. Miner, and P. E. Ciesielski, 1995: Circulations between mesoscale convective systems along a cold front. *Mon. Wea. Rev.,* **123,** 585–599.

Kessler, E., 1969: *On the Distribution and Continuity of Water Substance in Atmospheric Circulation. Meteor. Monogr.,* No. 32, Amer. Meteor. Soc., 84 pp.

Klemp, J. B., and R. B. Wilhelmson, 1978: The simulation of three-dimensional convective storm dynamics. *J. Atmos. Sci.,* **35,** 1070–1086.

Lamb, H., 1908: On the theory of waves propagated vertically in the atmosphere. *Proc. London Math Soc.,* **7,** 122–141.

——, 1932: *Hydrodynamics.* Dover, 738 pp.

Lighthill, M. J., 1978: *Waves in Fluids.* Cambridge University Press, 504 pp.

Mapes, B. E., 1993: Gregarious tropical convection. *J. Atmos. Sci.,* **50,** 2026–2037.

McAnelly, R. L., and W. R. Cotton, 1992: Early growth of mesoscale convective complexes: A meso-β-scale cycle of convective precipitation? *Mon. Wea. Rev.,* **120,** 1851–1877.

——, J. E. Nachamkin, W. R. Cotton, and M. E. Nicholls, 1997: Upscale evolution of MCSs: Doppler radar analysis and analytical investigation. *Mon. Wea. Rev.,* **125,** 1083–1110.

Nicholls, M. E., and R. A. Pielke, 1994a: Thermal compression waves. I: Total energy transfer. *Quart. J. Roy. Meteor. Soc.,* **120,** 305–332.

——, and ——, 1994b: Thermal compression waves. II: Mass adjustment and vertical transfer of total energy. *Quart. J. Roy. Meteor. Soc.,* **120,** 333–359.

——, ——, and W. R. Cotton, 1991a: Thermally forced gravity waves in an atmosphere at rest. *J. Atmos. Sci.,* **48,** 1869–1884.

——, ——, and ——, 1991b: A two-dimensional numerical investigation of the interaction between sea breezes and deep convection over the Florida peninsula. *Mon. Wea. Rev.,* **119,** 298–323.

——, ——, and R. N. Meroney, 1993: Large eddy simulation of microburst winds flowing around a building. *J. Wind Eng. Indus. Aerodyn.,* **46–47,** 229–237.

Pandya, R. E., and D. R. Durran, 1996: The influence of convectively generated thermal forcing on the mesoscale circulation around squall lines. *J. Atmos. Sci.,* **53,** 2924–2951.

——, ——, and C. Bretherton, 1993: Comments on ''Thermally forced gravity waves in an atmosphere at rest.'' *J. Atmos. Sci.,* **50,** 4097–4101.

Pielke, R. A., and Coauthors, 1992: A comprehensive meteorological modeling system—RAMS. *Meteor. Atmos. Phys.,* **49,** 69–91.

——, M. E. Nicholls, and A. J. Bedard, 1993: Using thermal compression waves to assess latent heating from clouds. *EOS,* **74,** 493.

Schmidt, J. M., and W. R. Cotton, 1990: Interactions between upper and lower atmospheric gravity waves on squall line structure and maintenance. *J. Atmos. Sci.,* **47,** 1205–1222.

Shaffer, J. A., R. S. Cerveny, and R. C. Balling Jr., 1997: Polar temperature sensitivity to lunar forcing? *Geophys. Res. Lett.,* **24,** 29–32.

Skamarock, W. D., and J. B. Klemp, 1992: The stability of time-split numerical methods for the hydrostatic and the nonhydrostatic elastic equations. *Mon. Wea. Rev.,* **120,** 2109–2127.

Tripoli, G. J., and W. R. Cotton, 1980: A numerical investigation of several factors leading to the observed variable intensity of deep convection over South Florida. *J. Appl. Meteor.,* **19,** 1037–1063.

——, and ——, 1982: The Colorado State University three-dimensional cloud/mesoscale model-1982. Part I: General theoretical framework and sensitivity experiments. *J. Rech. Atmos.,* **16,** 185–220.

——, and ——, 1986: An intense, quasi-steady thunderstorm over mountainous terrain. Part II: Three-dimensional numerical simulation. *J. Atmos. Sci.,* **43,** 896–914.

Walko, R. L., W. R. Cotton, M. P. Meyers, and J. Y. Harrington, 1995: New RAMS cloud microphysics parameterization. Part I: The single-moment scheme. *Atmos. Res.,* **38,** 29–62.

Wallace, J. M., and P. V. Hobbs, 1977: *Atmospheric Science: An Introductory Survey.* Academic Press, 467 pp.